The scientific impact of the LAMOST on stellar astronomy

Joanna Molenda-Żakowicz
University of Wrocław, Poland

2nd LAMOST-Kepler workshop, Royal Observatory of Belgium, 1 Aug 2017

The LAMOST –Kepler workshops: Beijing 2014 and Brussels 2017

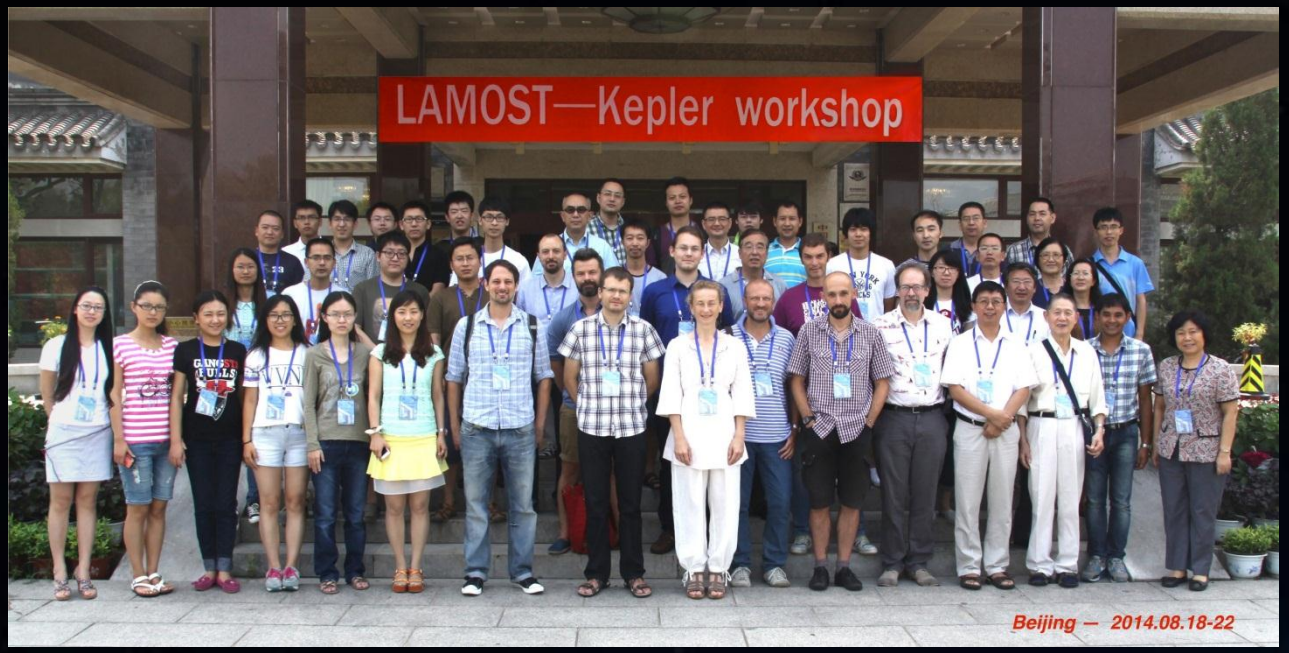

„The scientific impact of the LAMOST on stellar astronomy", Joanna Molenda-Żakowicz, 2nd LAMOST-Kepler workshop, 1 Aug 2017, Brussels, Belgium.

Stars: fundamental parameters

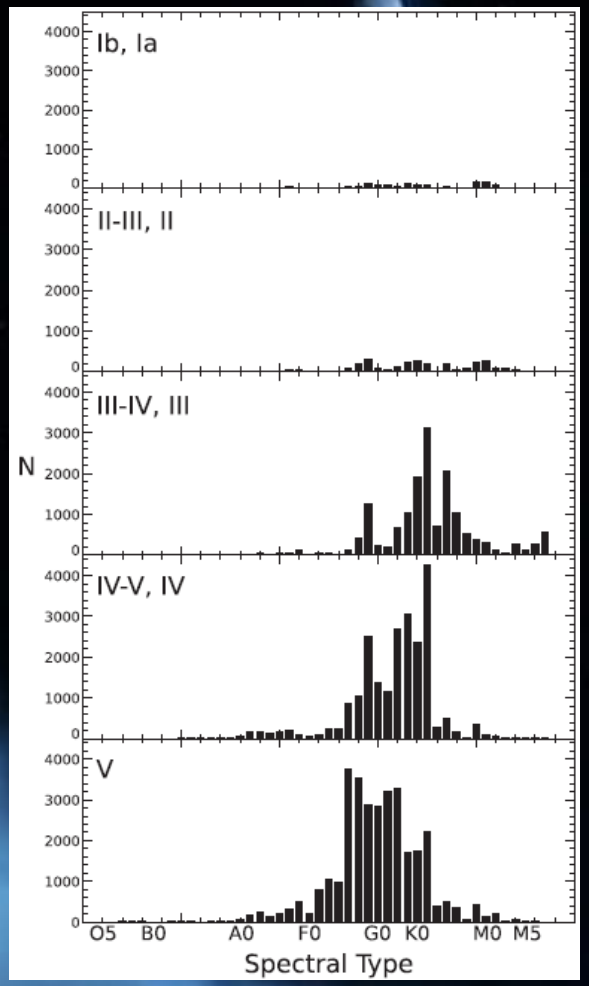

The frequency of the spectral types of 81,171 targets, organized vertically by luminosity class (Gray et al. 2016).

LAMOST-Kepler project: round 1

- 101,086 spectra acquired between 2011 and 2014 (De Cat et al. 2015),
- T_{eff}, log g, [Fe/H], and RV derived from 61,753 spectra of 51,385 stars (Frasca et al. 2016).

Talks by Antonio Frasca, Anbing Ren, Richard O. Gray & Chris Corbally

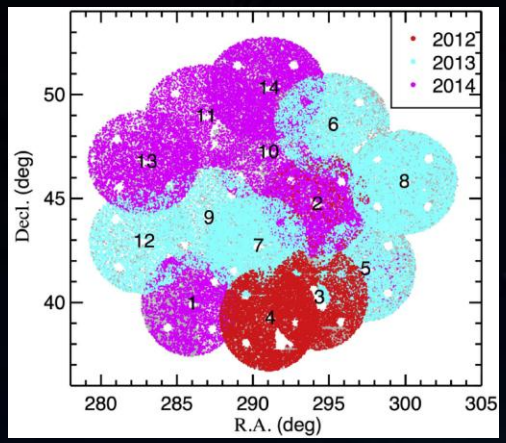

51,406 stars for which the atmospheric parameters were derived with the LAMOST Stellar Parameter pipeline LASP (Ren et al. 2016).

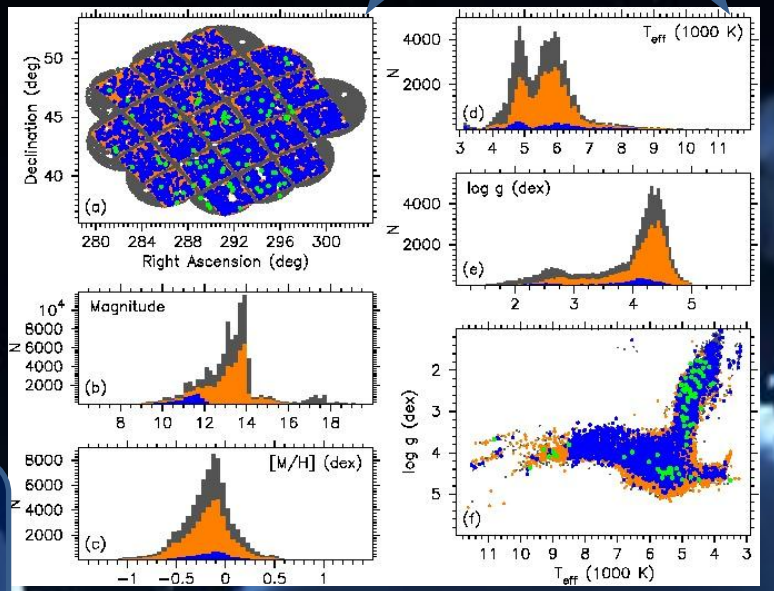

De Cat et al. (2015)

KIC atmospheric parameters

Stars: fundamental parameters

The Kepler Input Catalogue (KIC) metallicities are biased:

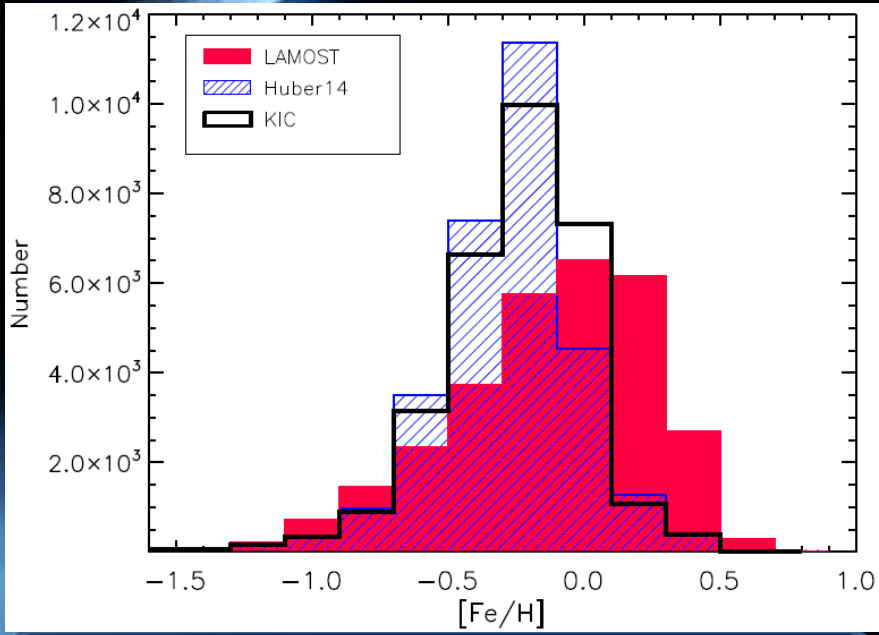

The [Fe/H] distribution of 30,104 stars for the LAMOST-Kepler subsample of stars in common with the Huber et al. (2014) catalog. The metallicities from the KIC catalog are shown with the empty histogram (Frasca et al. 2016).

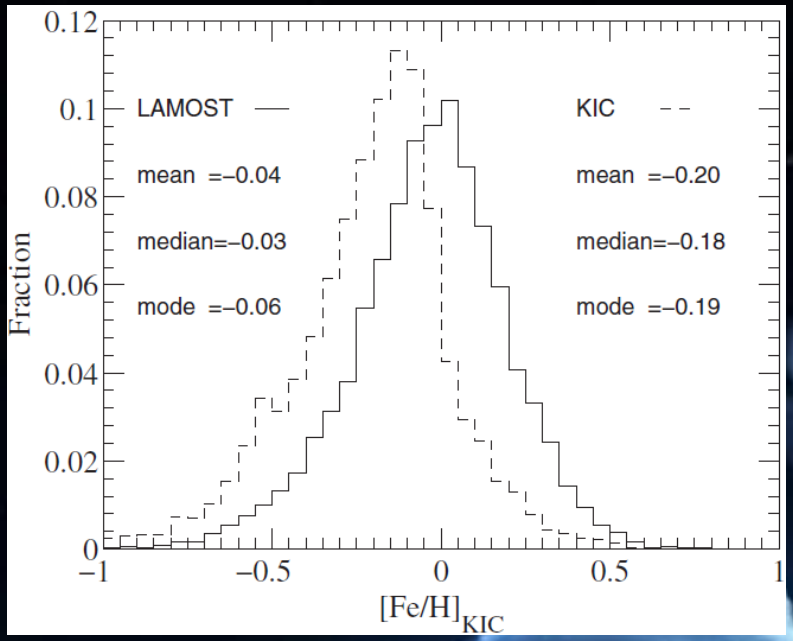

Metallicity distribution of the sample of 12,000 stars. Solid: LAMOST [Fe/H]; dashed: KIC [Fe/H] (Dong et al. 2014).

Stars: fundamental parameters

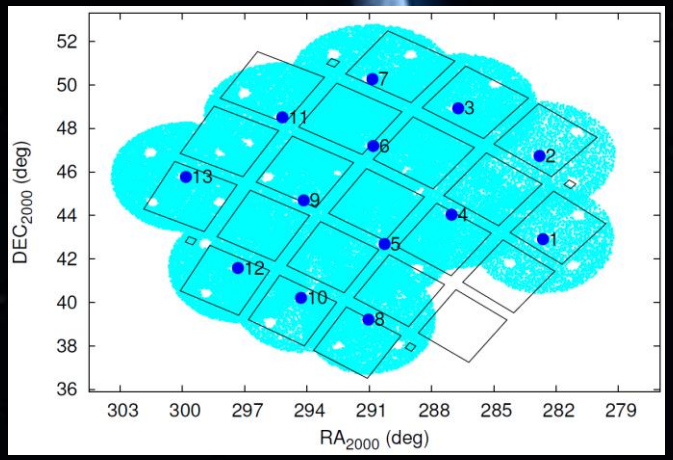

LAMOST-Kepler project: round 2

- Started in 2015 when we acquired 97,641 spectra of 86,378 individual stars (Molenda-Żakowicz et al. 2017),
- The missing 14th field and the sparsely sampled areas were scheduled for observing in 2016 but they have been postponed for 2017 because of bad weather conditions at the Xinglong Observatory.
- The LAMOST-Kepler round 2 was completed in 2017.

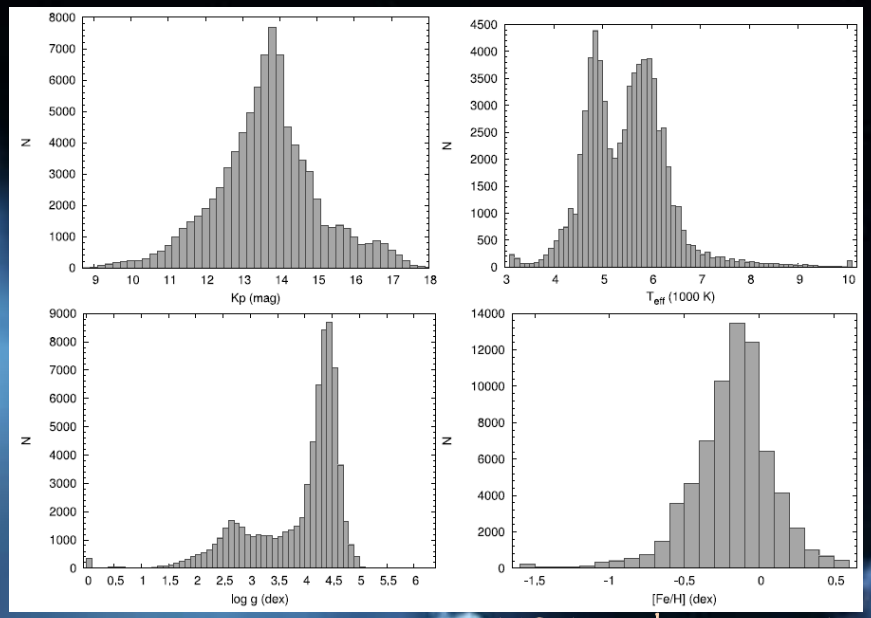

KIC atmospheric parameters

Field	R.A. (2000)	DEC (2000)	Date	Number of exposures	Number of spectra
1	18:50:31	42:54:43	2015-10-04	1	3090
2	18:51:11	46:44:17	2015-10-06	1	2947
3	19:06:51	48:55:31	2015-05-30	3	7853
,,	,,	,,	2015-09-15	1	3084
4	19:08:08	44:02:10	2015-09-25	2	6153
5	19:21:02	42:41:13	2015-10-11	2	6223
6	19:23:14	47:11:44	2015-09-14	1	3140
,,	,,	,,	2015-10-02	2	6251
7	19:23:23	50:16:16	2015-05-29	2	5517
,,	,,	,,	2015-09-13	1	3169
8	19:24:09	39:12:42	2015-10-12	2	6303
9	19:36:37	44:41:41	2015-09-21	3	9163
10	19:37:08	40:12:49	2015-10-18	1	3120
11	19:40:45	48:30:45	2015-09-16	1	3135
,,	,,	,,	2015-10-01	2	6314
12	19:49:18	41:34:56	2015-10-08	3	9454
13	19:59:20	45:46:21	2015-09-18	2	6350
,,	,,	,,	2015-10-03	2	6375
					Total: 97,641

Stars: fundamental parameters

Talk by
Ruyuan Zhang

LAMOST observes the northern K2 fields

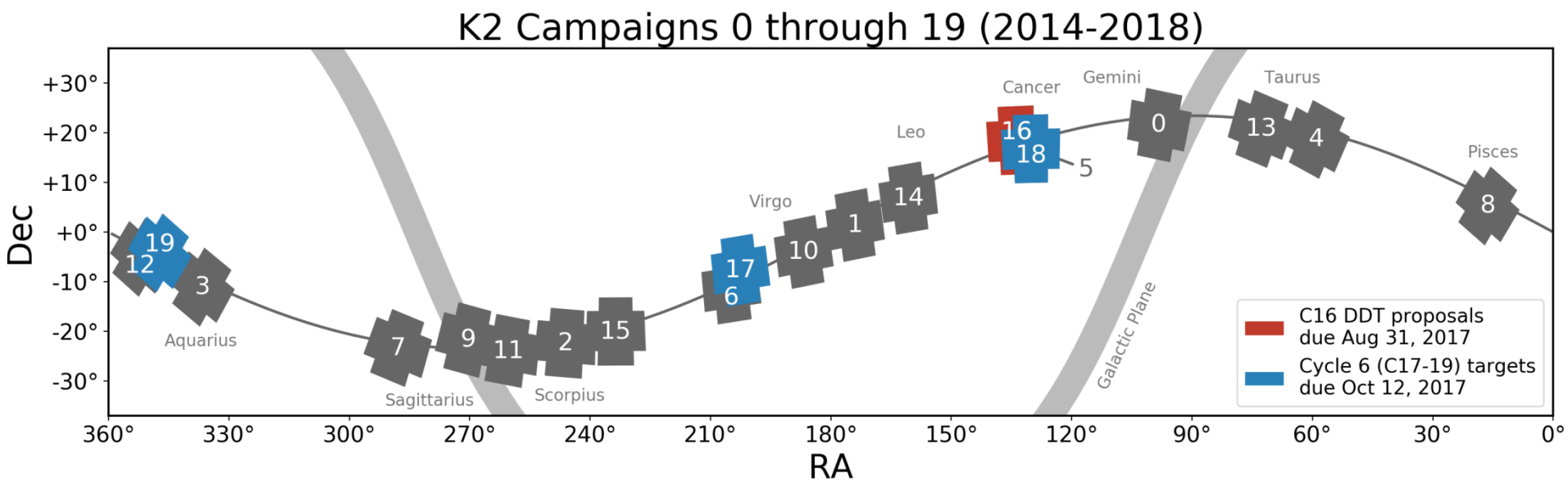

Stars: asteroseismology

Talks by
Filiz Kahraman Alicavus,
Ceren Ulusoy,
Weikai Zong,
Mengqi Jin,
Jie Yu

Types of pulsating stars targeted by LAMOST: δ Sct, chemically peculiar stars, compact pulsators and many others. Among them there are solar-type stars:

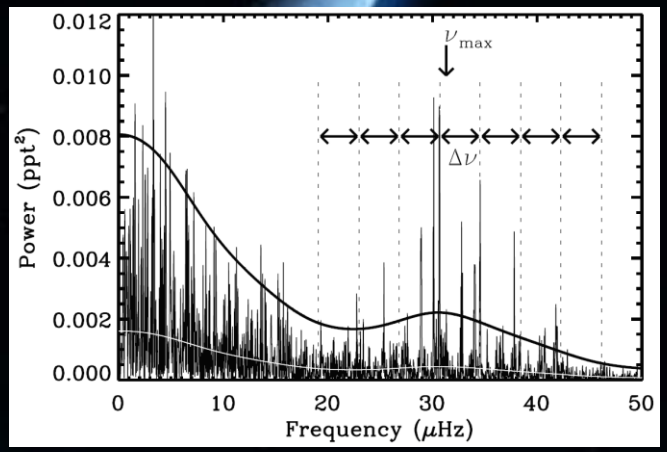

Power spectrum of KIC2436824. The average large frequency separation, $\Delta\nu$, and the frequency of maximum power, ν_{max}, are indicated by arrows (Stello et al. 2011).

$$\nu_{max} \simeq \frac{M/M_\odot (T_{eff}/T_{eff,\odot})^{3.5}}{L/L_\odot} \nu_{max,\odot}$$

$$\Delta\nu \simeq \frac{(M/M_\odot)^{0.5} (T_{eff}/T_{eff,\odot})^{3}}{(L/L_\odot)^{0.75}} \Delta\nu_\odot$$

T_{eff} = 5777 K, ν_{max} = 3100μHz, $\Delta\nu$ = 135 μHz

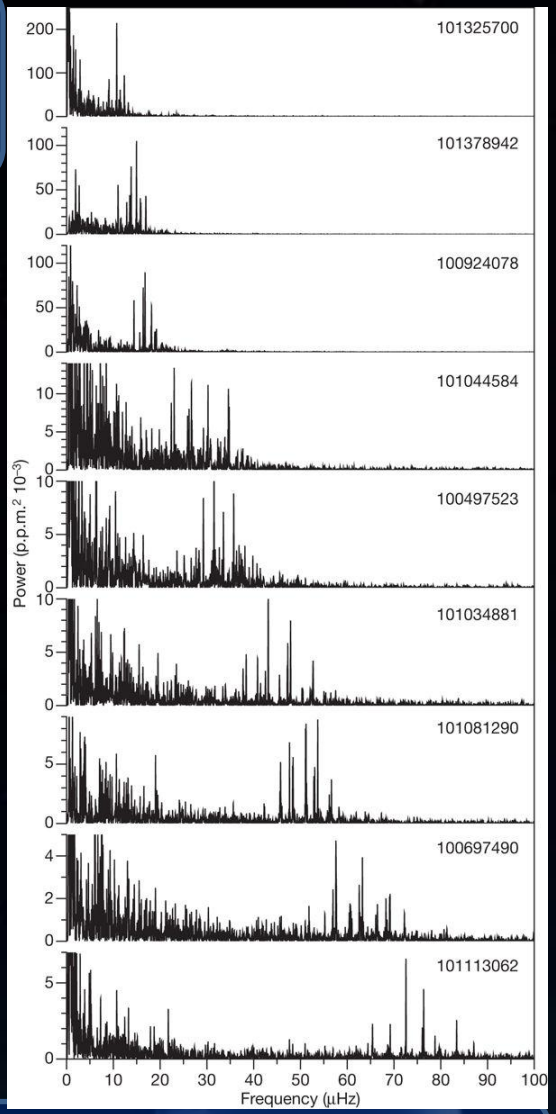

A stack of power spectra of nine red giant pulsators (De Ridder et al. 2009).

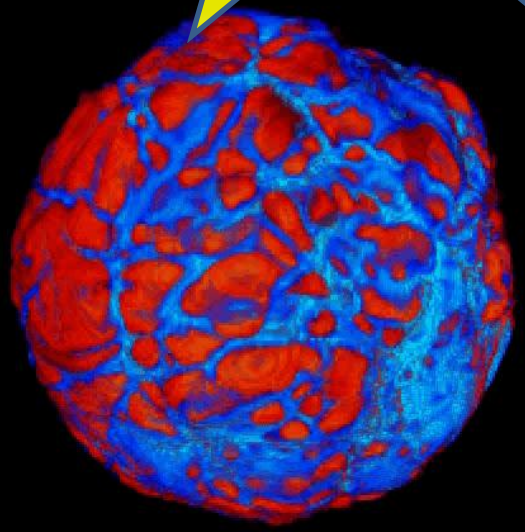

Pulsating red giant star. Warm temperatures are red and yellow, while relatively cool temperatures are blue and aqua (David Porter, Sarah Anderson, and Paul Woodward of the University of Minnesota's Laboratory for Computational Science & Engineering).

Stars: asteroseismology

- Revised stellar properties for 197,096 Kepler targets observed between Quarters 1–17 DR25 (Mathur et al. 2017).
- The catalog includes the fundamental parameters, distances, extinctions, radii and masses of Kepler targets .

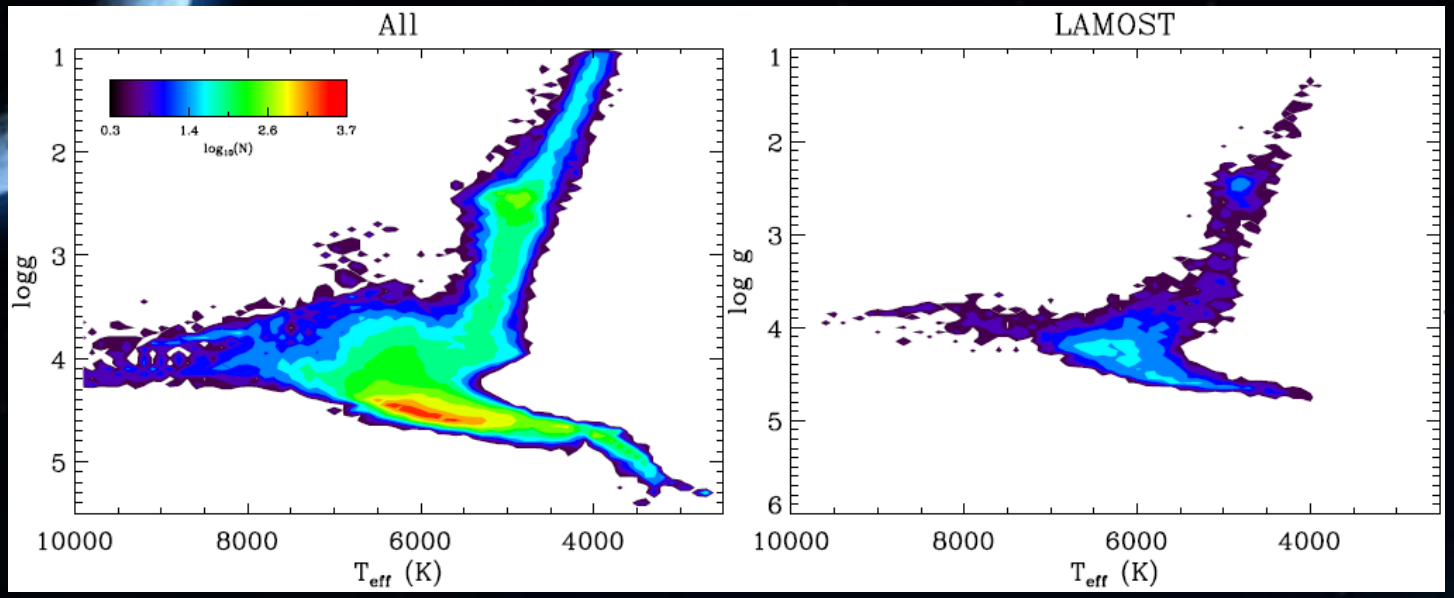

Input surface gravity and effective temperature for the full catalog. LAMOST is the largest of the new sources of the input values (Mathur et al. 2017).

Table 4

Output values of the DR25 stellar properties catalog with the updated distances and extinctions.

KIC	$T_{\rm eff}$	$\log g$	[Fe/H]	R	M	ρ	d (kpc)	A_V
757076	5160^{+171}_{-156}	3.580 ± 0.232	$-0.100^{+0.300}_{-0.300}$	$3.13^{+0.99}_{-2.30}$	$1.36^{+0.20}_{-0.48}$	$0.06^{+1.81}_{-0.04}$	$0.52^{+0.13}_{-0.30}$	$0.32^{+0.08}_{-0.24}$
757099	5519^{+182}_{-149}	3.822 ± 0.213	$-0.220^{+0.350}_{-0.250}$	$2.11^{+0.67}_{-1.25}$	$1.08^{+0.17}_{-0.23}$	$0.16^{+1.70}_{-0.08}$	$0.75^{+0.17}_{-0.34}$	$0.43^{+0.06}_{-0.24}$
757137	4706^{+74}_{-102}	2.374 ± 0.027	$-0.100^{+0.200}_{-0.300}$	$15.45^{+3.54}_{-3.93}$	$2.06^{+1.16}_{-0.95}$	$0.00^{+0.00}_{-0.00}$	$0.66^{+0.13}_{-0.14}$	$0.39^{+0.06}_{-0.10}$

Variable u-band sources

- Application of LAMOST to classification of variable u-band sources.
- 82 u-band variable objects based on the u-band photometry data from South Galactic Cap u-band Sky Survey (SCUSS) and Sloan Digital Sky Survey (SDSS) (Tian-Wen Cao et al. 2016).
  - The magnitude variation: larger than 0.2 mag.
  - Limiting magnitude down to 19.0 mag in u-band.
- According to the spectra from LAMOST, there are 11 quasars, 60 variable stars and 11 unclassified targets.
- The variable stars include one active M-type dwarf, seven Horizontal Branch stars, one giant, one AGB star and two newly discovered RR Lyrae candidates.

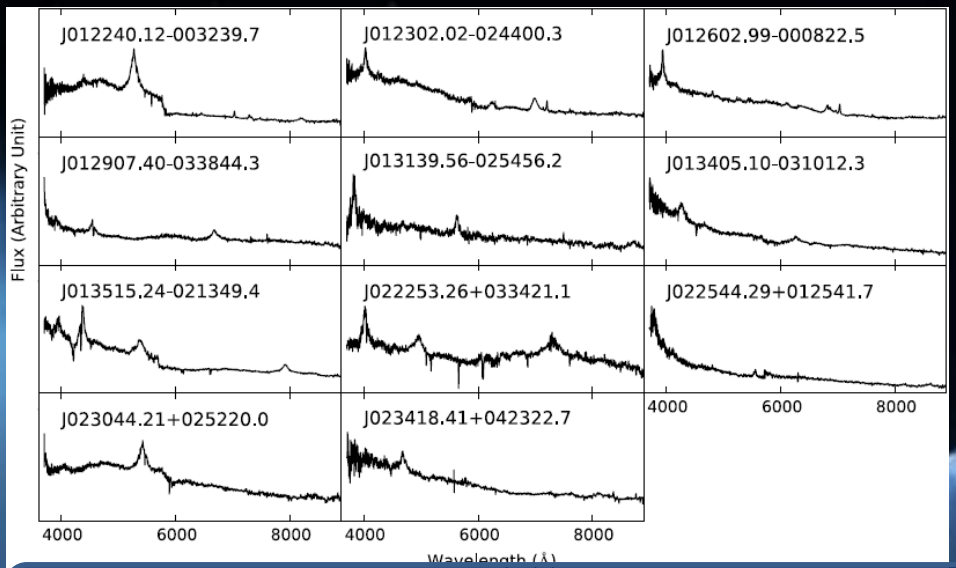

The quasars were identified by their broad band emission lines: [CIV] λ1549, [CIII] λ1909, MgII λ2800, Hγ λ4340, Hβ λ4861, and Hα λ6563. The spectra of 11 variable quasars. Seven are new sources (Tian-Wen Cao et al. 2016).

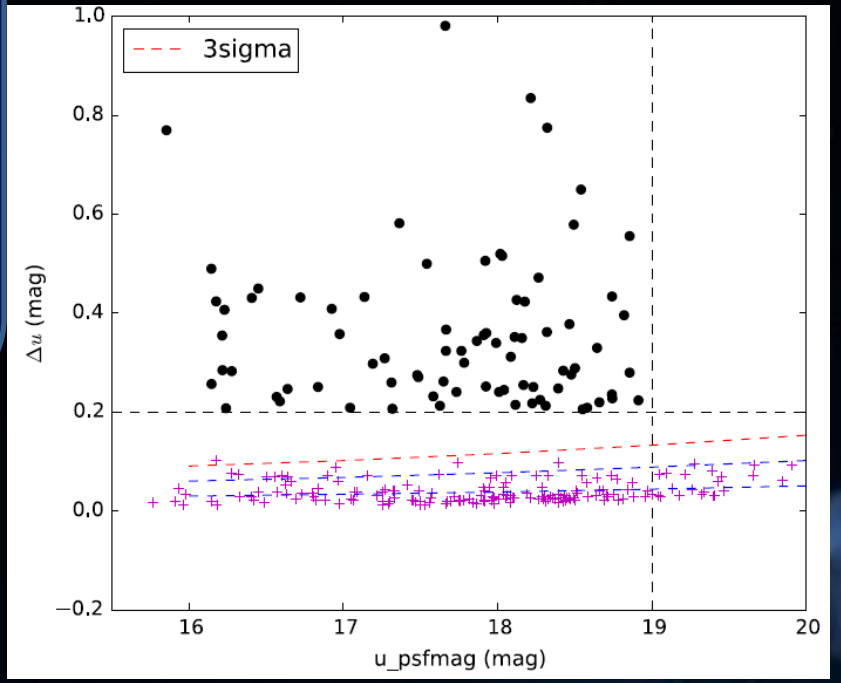

Diagram of magnitudes versus variation in u-band. The plus signs (+) represent the standard deviation (σ) of magnitude variation. The *red dashed line* represents the fitting of 3-σ errors by second order polynomial. The *black dots* represent 82 u-band variable objects. The *dashed lines* are selection criteria: u <19 mag and Δu > 0.2 mag (Tian-Wen Cao et al. 2016).

Variable u-band sources

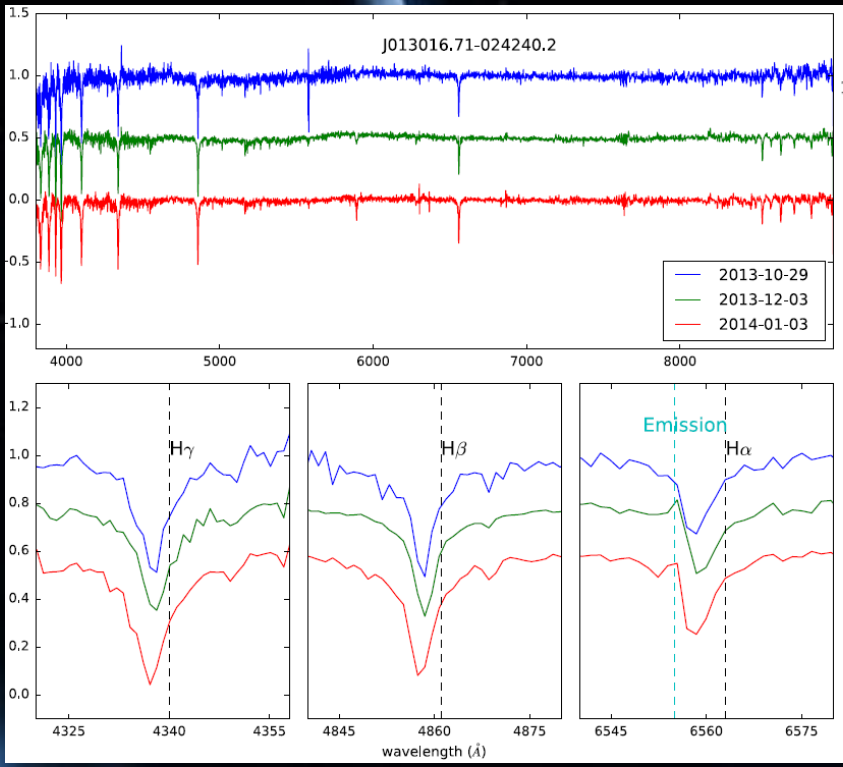

Three normalized spectra of one of the RR Lyr stars The *bottom panels* show the Balmer absorption lines. The *vertical black dashed lines* show the rest-frame wavelength of the spectral lines. The *vertical blue dashed line* in the *right picture* shows the position of fill-in Hα emission (Tian-Wen Cao et al. 2016).

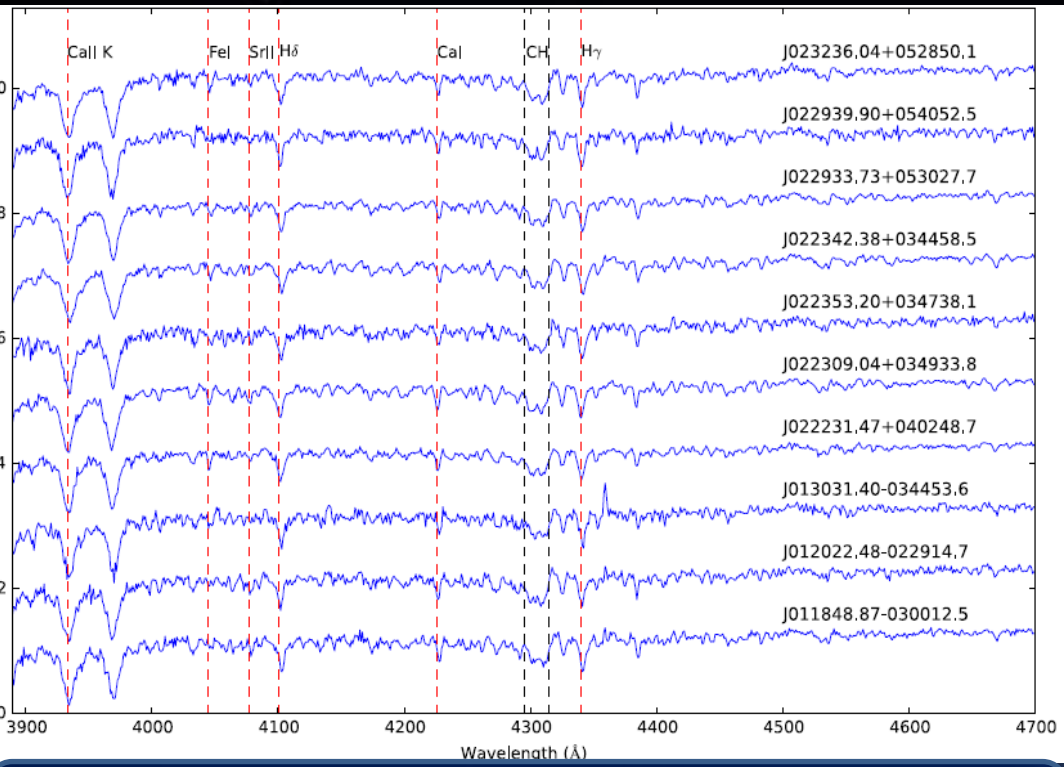

The spectra of 10 late F-type or early G-type stars. The feature of molecule CH (from λ4295 to λ4315) is wide, and shown between two *black dashed lines*. The *red lines* represent positions of other lines (Tian-Wen Cao et al. 2016).

Open clusters: NGC 6866

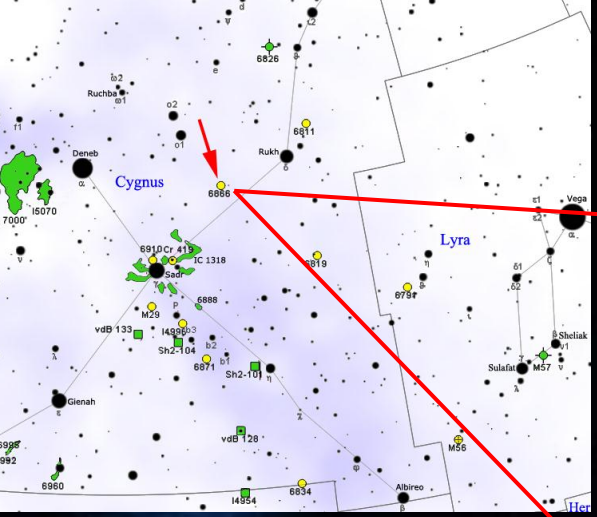

Bostanci et al. (2015) found 31 stars in the field of NGC 6866 in the LAMOST database for which atmospheric parameters and radial velocities were measured.

Photometric and astrometric analysis was performed for 1301 stars with V < 18mag.

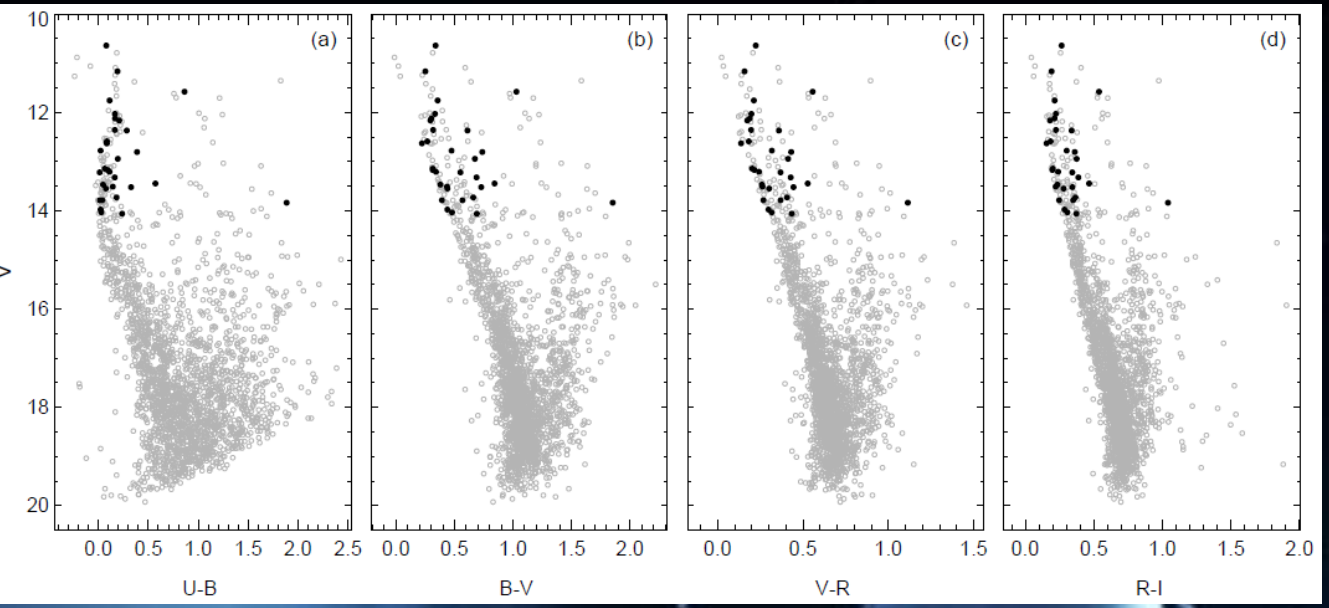

The CMDs for the cluster NGC 6866. Black dots represent the stars with LAMOST spectra (Bostanci et al. 2015).

Open clusters: NGC 6866

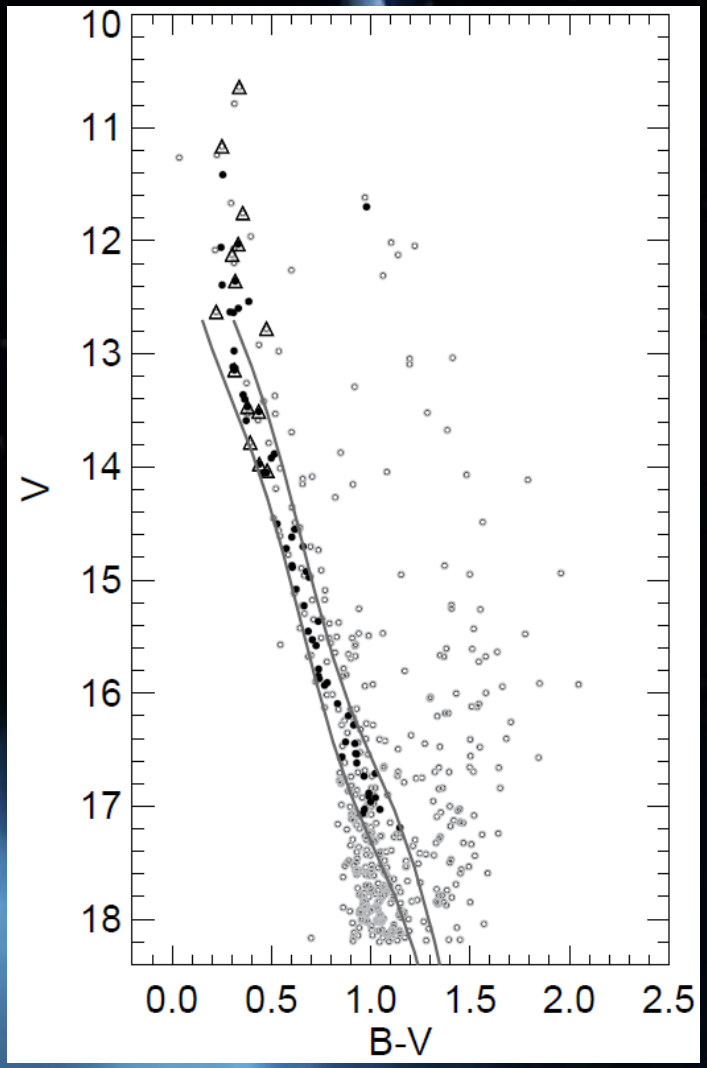

V vs B−V CMD of NGC 6866 for stars which are located in a circle of 6 arc min radius from the center of the cluster. Solid lines represent the ZAMS. Black dots denote the most probable cluster stars. Open triangles indicate the stars with LAMOST spectra (Bostancı et al. 2015).

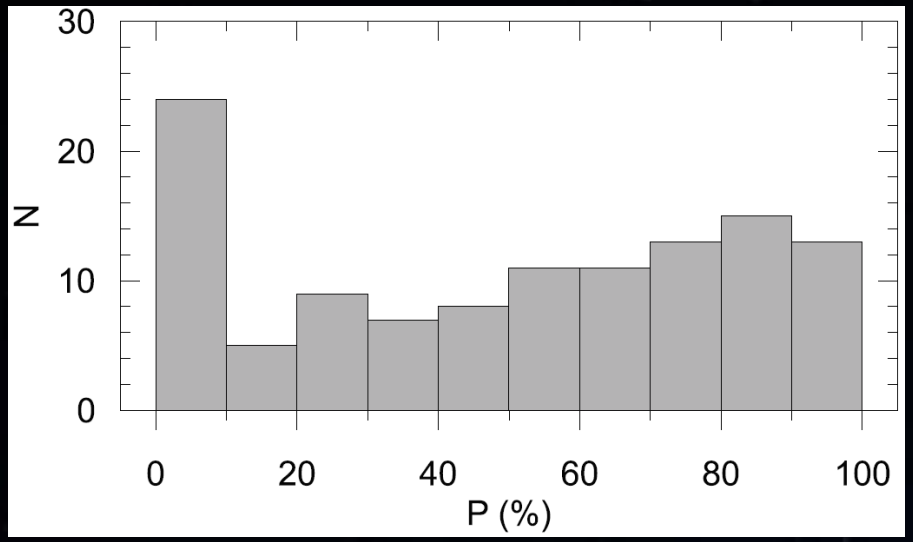

The histogram of the membership probabilities estimated for the stars which are located in a circle with a radius of 6 arc min from the center of NGC 6866 (Bostancı et al. 2015).

Color excesses:
$E(U-B) = 0.054 \pm 0.036$ mag
$E(B-V) = 0.074 \pm 0.050$ mag.

Open clusters: NGC 6866

KIC	P (%)	T_{eff} (K)	$\log g$ (cgs)	$[Fe/H]$ (dex)	V_r (km s^{-1})
8197761	00	7153±77	4.02±0.32	-0.04±0.09	-29.12±24.47
8264534	27	8270±83	3.87±0.34	-0.03±0.10	-6.48±20.51
8264674	36	8232±59	3.86±0.32	-0.12±0.08	9.47±20.87
8264698	61	7730±64	3.98±0.35	-0.15±0.13	12.92±32.76
8264949	00	7726±53	3.89±0.34	-0.16±0.11	11.59±29.85
8264148	40	6977±152	4.09±0.33	-0.06±0.16	14.10±22.80
8264581	90	7337±113	3.66±0.38	0.62±0.10	10.25±17.00
8264037	00	7244±92	3.97±0.36	-0.04±0.11	5.29±29.05
8330790	94	7669±69	4.05±0.33	-0.09±0.13	-22.79±32.92
8264617	76	7177±139	4.11±0.32	-0.20±0.16	10.90±25.28
8265068	75	7570±50	3.98±0.31	-0.11±0.11	13.59±30.90
8264075	17	7177±152	4.11±0.34	-0.12±0.17	10.60±26.74
8197368	20	6622±107	4.24±0.35	-0.08±0.11	4.79±22.63
8330778	53	7268±130	3.99±0.47	-0.09±0.19	8.45±59.52

Stars with the LAMOST spectra which are located in a circle of 6 arc min radius from the center of the cluster were used to derive the mean radial velocity and the metallicity of the cluster (Bostancı et al. 2015). Six stars out of 14 have the membership probabilities larger than 50%. Using those six stars Bostancı et al. (2015) calculated the median metallicity and the radial velocity of NGC 6866: [Fe/H] = −0.10 ± 0.13 dex and Vr = 10.58 ± 31.83 km s^{-1}

d (distance)= 1189 ± 75 pc t (age) = 813 ± 50 Myr
R_{max} (apogalactic dist.) = 9.78 kpc, R_{min} (perigalactic dist.) = 7.76 kpc
Z_{max} (maximum vertical distance from the Galactic plane)= 160 pc.
e (eccentricity of the orbit) = 0.12
P_{orb} (galactic period) = 156 Myr

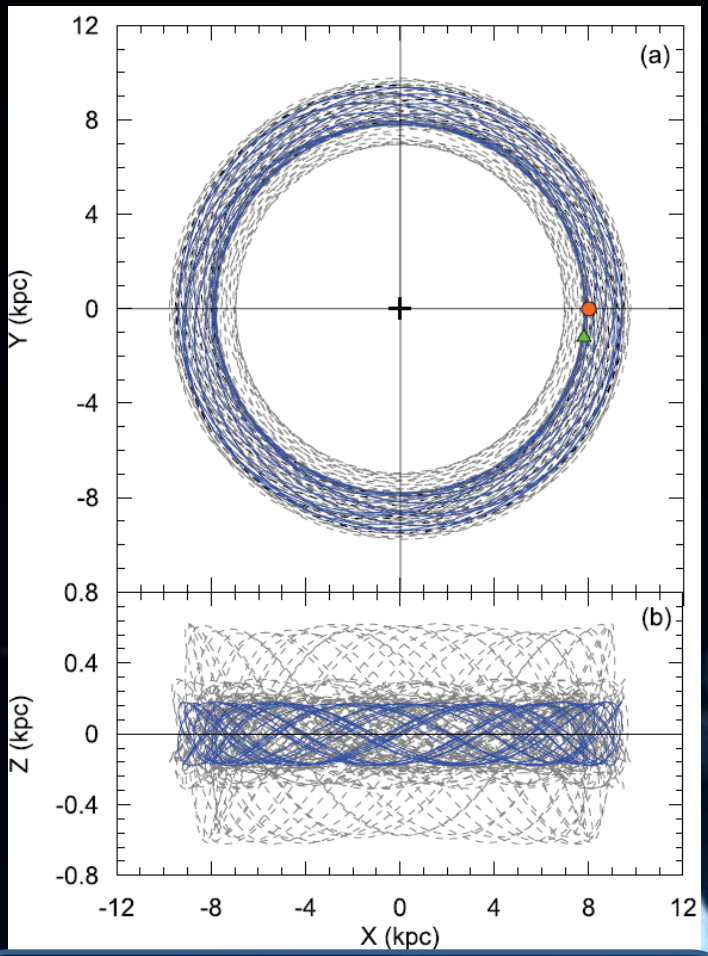

The Galactic orbital motions (grey dashed lines) of the six cluster stars with P > 50%, for which LAMOST spectra are available, in the X − Y (a) and X − Z (b) planes. The cluster's mean orbit is indicated with a blue line. The black plus, red circle and green triangle symbols in panel (a) represent the Galactic center, and current locations of the Sun and NGC 6866, respectively (Bostancı et al. 2015).

Members of the Milky Way star clusters

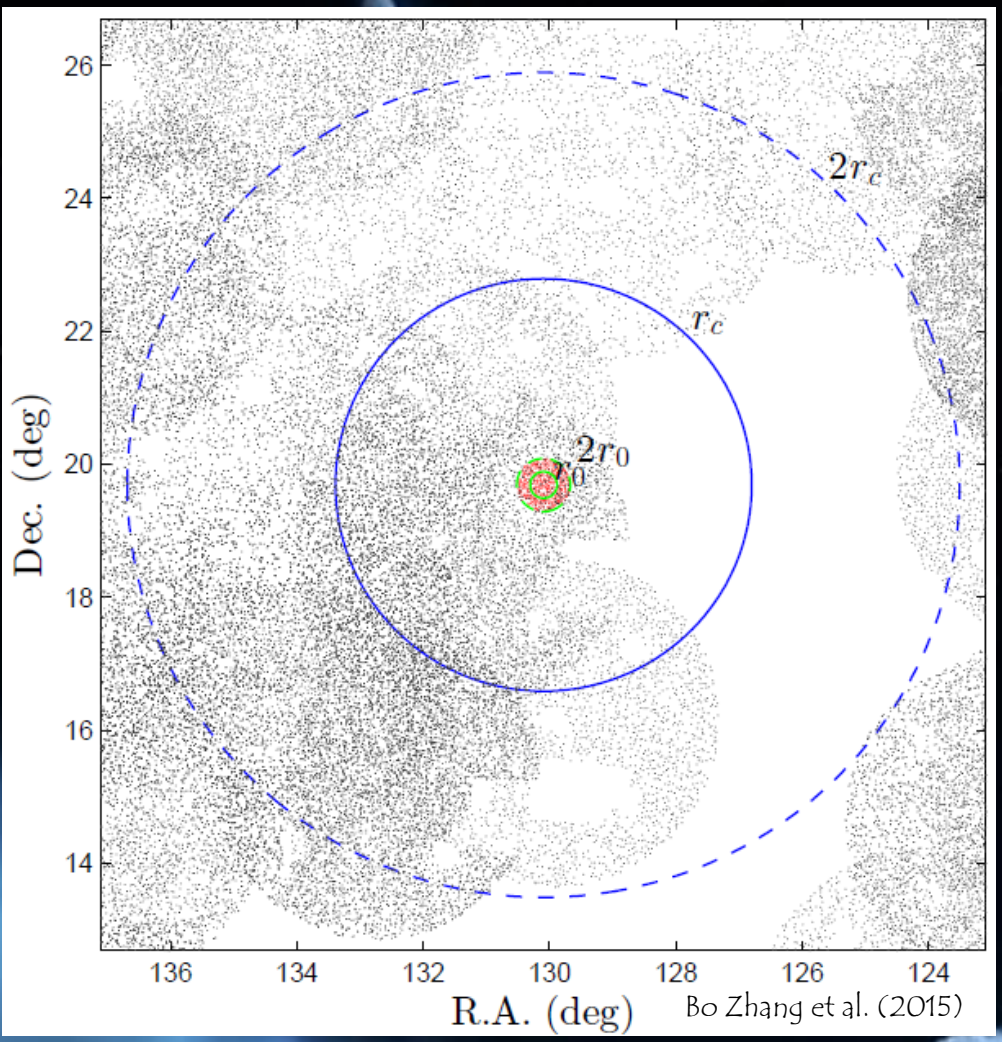

Bo Zhang et al. (2015)

The LAMOST DR2 catalog contains 4,136,482 targets including:

- 3,784 ,61 stars,
- 37,206 galaxies,
- 8,630 QSOs,
- 306,185 unknown objects.

For 2,207,788 stars the values of T_{eff}, logg, [Fe/H], and RV have been derived with LASP.

In total, 457 star clusters, including open clusters, globular clusters, stellar associations and moving groups, are included in LAMOST DR2.

Bo Zhang et al. (2015) adopted the Milky Way Star Cluster (MWSC) catalog (Kharchenko et al. 2012, 2013) as the list of target star clusters since it provides homogeneous parameters of Milky Way star clusters and is complete in the volume observed by LAMOST.

A sample cluster NGC 2632 (M44). The circle traced by the green (*blue*) solid line represent, respectively, the angular radius of the core of the cluster (r_0) and the angular radius of the clusterand the (r_c).Each circle drawn with a dashed line has a radius twice that of the solid line circle with the same color. The red dots indicate UCAC4/Pan-STARRS1 data in the circle drawn with a green dashed line (within 2 r_0) and black dots denote stars observed by LAMOST. The red dots in the green dashed circle are selected to highlight the intrinsic stellar locus of the cluster.

Members of the Milky Way star clusters

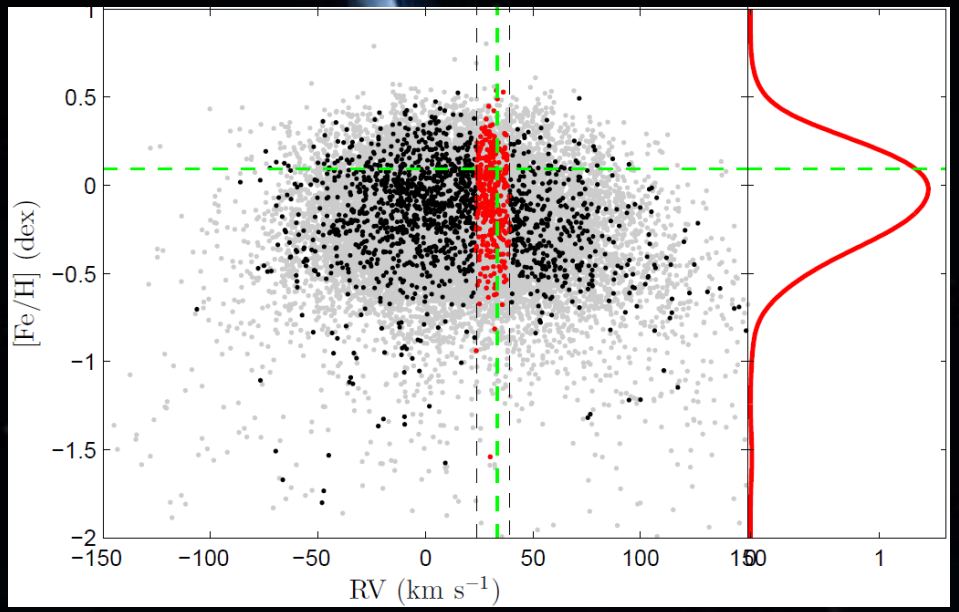

The kinematic member identification for NGC 2632. The gray and black dots are stars located within $2r_c$ of the center of the cluster with and without CMD selection respectively. The candidate members selected using the distribution of RV are represented as red.

The right panel shows the kernel smoothed distribution of [Fe/H] for the candidates (red dots in the bottom panel) smoothed by a Gaussian kernel with a bandwidth of 0.12 dex (typical error). The kinematically selected candidate members show a significant peak around the green horizontal line, which is the metallicity of the cluster from the MWSC catalog. (Bo Zhang et al. 2015).

RV distribution is the best discriminator of cluster membership because it has the smallest relative measurement errors.

Although [Fe/H] can be used in identification of the members, it may not significantly improve the performance since most of the open clusters have very similar metallicity as the field stars and the measurement error of 0.1-0.2 dex is much larger than the intrinsic dispersion.

Members of the Milky Way star clusters

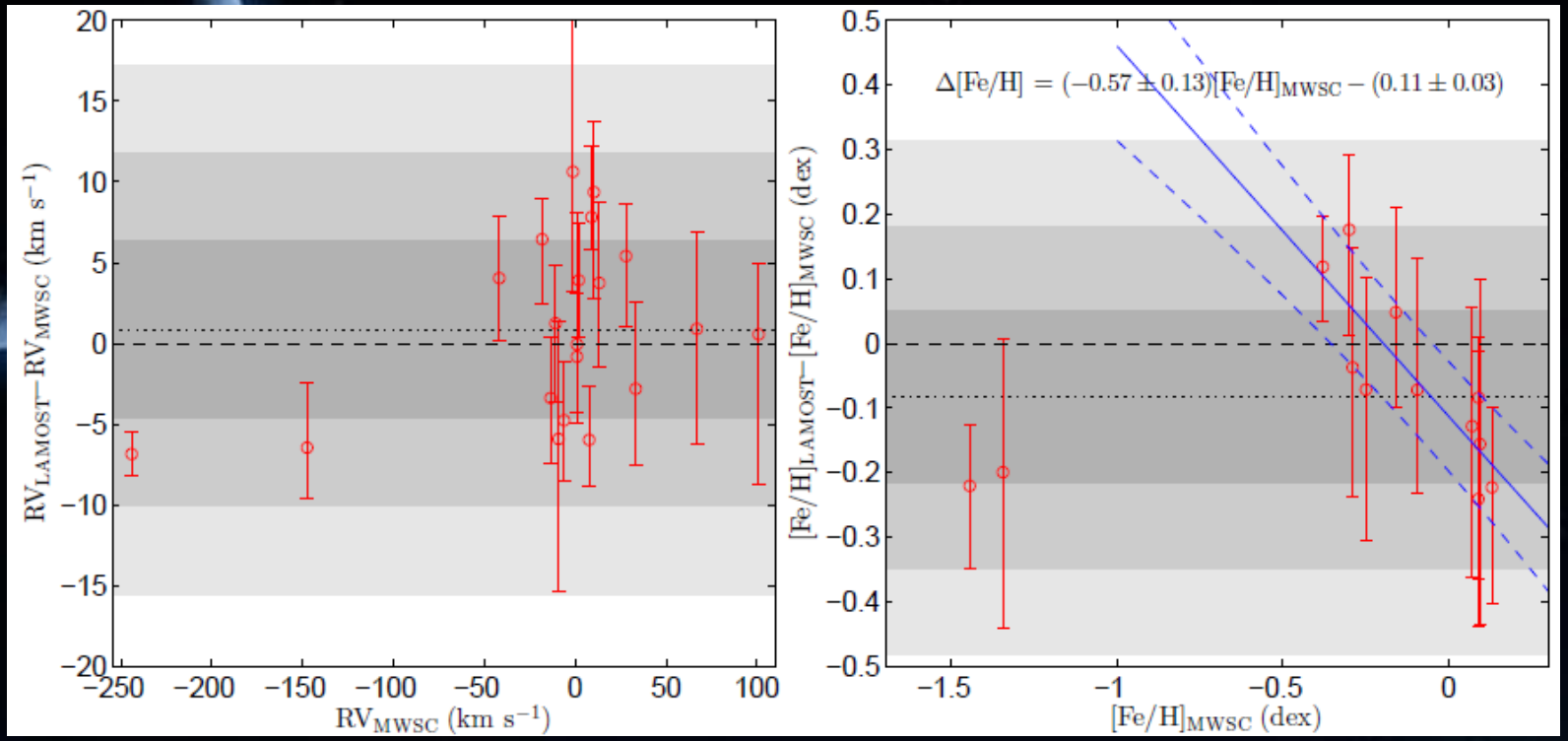

Bo Zhang et al. (2015) provided a list of clusters with at least three kinematic candidate members, which includes 21 open clusters, 2 globular clusters and 1 open cluster with nebulosity. They identified 2189 candidate members from the kernel-smoothed distribution of RV and 3559 from RVz.

The figure shows a comparison of RV and [Fe/H] derived by Bo Zhang et al. (2015) for the cluster with the literature values shows a systematic offset in RV: 0.85 km s^{-1}, with a dispersion of 5.47 kms^{-1}.

For [Fe/H] the offset and dispersion are −0.08 dex and 0.13 dex. The LAMOST [Fe/H] is not consistent with values from the MWSC. This is possibly due to both the contributions from contamination of field stars in our candidate member stars and the biased metallicity estimated by LASP.

Halo stars of the galactic globular clusters M3 and M13

Navin et al. (2016) performed a search for members and extratidal cluster halo stars within and outside of the tidal radius of these clusters in the LAMOST Data Release 1.

Globular clusters lose stars through both internal processes and external influences:

- stellar evolution,
- two-body relaxation,
- tidal disruption,
- dynamical friction,
- gravitational shocks due to passages close to the bulge and through the disks of their host galaxies.

The existence and properties of these extratidal stars can tell us:

- How a globular cluster evolved since its formation,
- Help to understand the initial properties of the Galactic globular clusters system
  - Gnedin & Ostriker (1997) concluded that the surviving population of globular clusters was a small fraction of those originally formed, and that a large fraction of the stars in the Galactic bulge and halo originated in globular clusters .
  - Mackey & Gilmore (2004) estimated that ~100 of the present Milky Way globular clusters population were formed in the Galaxy and calculated that at least 50% of the clusters have been destroyed over the last Hubble time.
- What are the properties of the host galaxy
  - The lost stars contribute to a galaxy's stellar population,
  - The tidal tails may be used as tracers of the galactic gravitational potential,
  - They can be an indicator of the formation history of the host galaxy (some globular clusters are believed to be part of dwarf galaxies that are accreted).

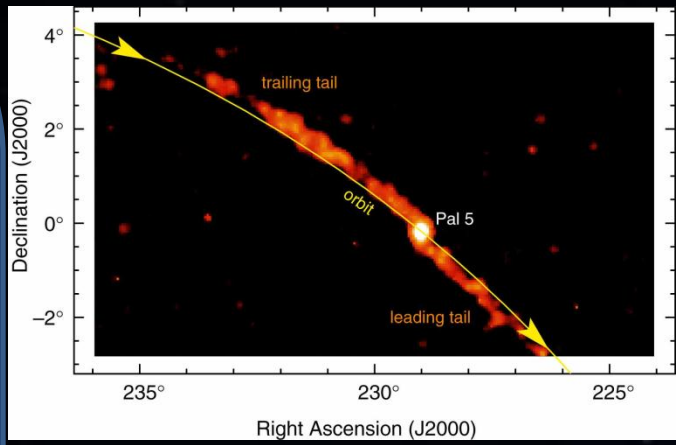

Distribution of stars emerging from the star cluster Palomar 5 (white blob). The two long tidal tails (orange) contain 1.3 times the mass of the cluster and delineate its orbit around the Milky Way (yellow line). (Sloan Digital Sky Survey SDSS)

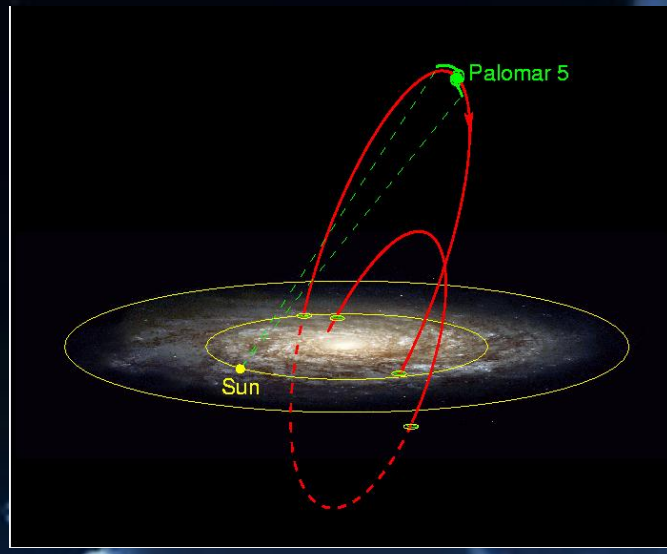

Halo stars of the galactic globular clusters M3 and M13

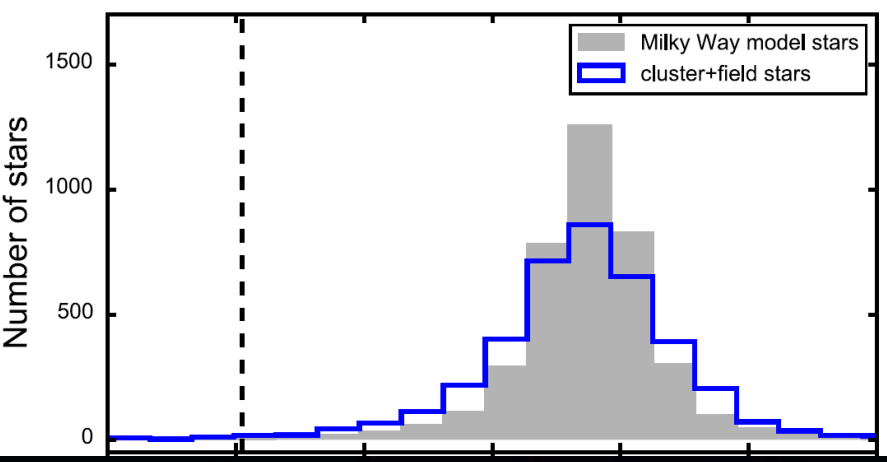

Navin et al. (2016)

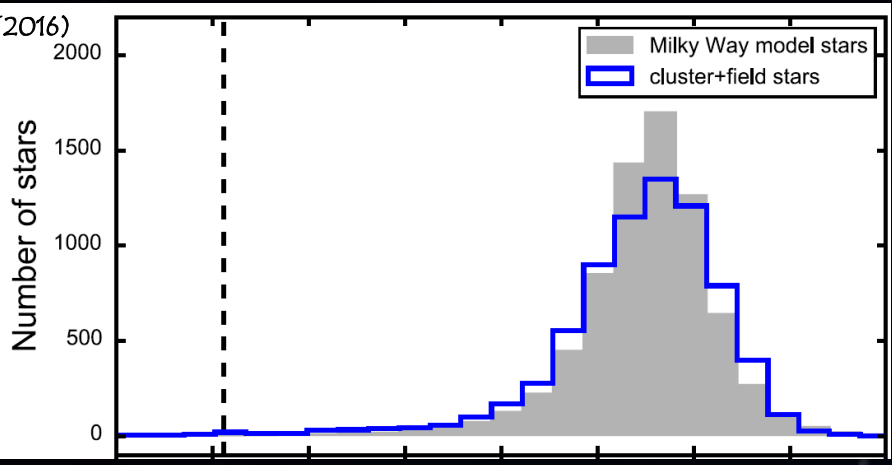

The Vr histograms of the stars observed within a radius of 5° of the clusters' central positions with the predicted Vr distribution of the Milky Way model generated by the Galaxia code (Sharma et al. 2011) overplotted as a gray histogram. The vertical dashed line shows the GC Vr.

M3: 4426 entries in the DR1 Catalog within a radius of 5° of the central position of the cluster

- 3879 unique stars,
- Literature $V_r = -147.6 \pm 0.2$ km s^{-1} ,
- 50 stars in DR1 Catalog have V_r within $\pm 2\sigma$ of the GC V_r and fall inside a radius of 5° of the GC central position,

M13: 8265 entries in the DR1 Catalog within a radius of 5° of the central position of the cluster

- 7355 unique stars,
- Literature $V_r = -244.2 \pm 0.2$ km s^{-1} ,
- 61 stars in DR1 Catalog have V_r within $\pm 2\sigma$ of the GC V_r and fall inside a radius of 5° of the GC central position.

Cluster members and extratidal halo stars should share the Vr signature of the GC; proper motions and [Fe/H] were not used to eliminate the candidate members.

Halo stars of the galactic globular clusters M3 and M13

Left-hand panel: spatial distribution of DR1 Catalog stars around M3. Right-hand panel: expanded version showing the DR1 Catalog stars inside the tidal radius. Gray crosses show non-members, and red triangles denote candidate cluster member stars and candidate extratidal cluster halo stars. The green cross and solid circle show the center position and the tidal radius, respectively; the dashed circle is at a 5° radius from the center position. The black dotted arrow indicates the direction of the cluster proper motion, the blue dashed arrow is the direction to the Galactic center, and the solid red arrow is the direction perpendicular to the Galactic plane.

The eight stars outside the adopted tidal radius are identified as candidate extratidal cluster halo stars.

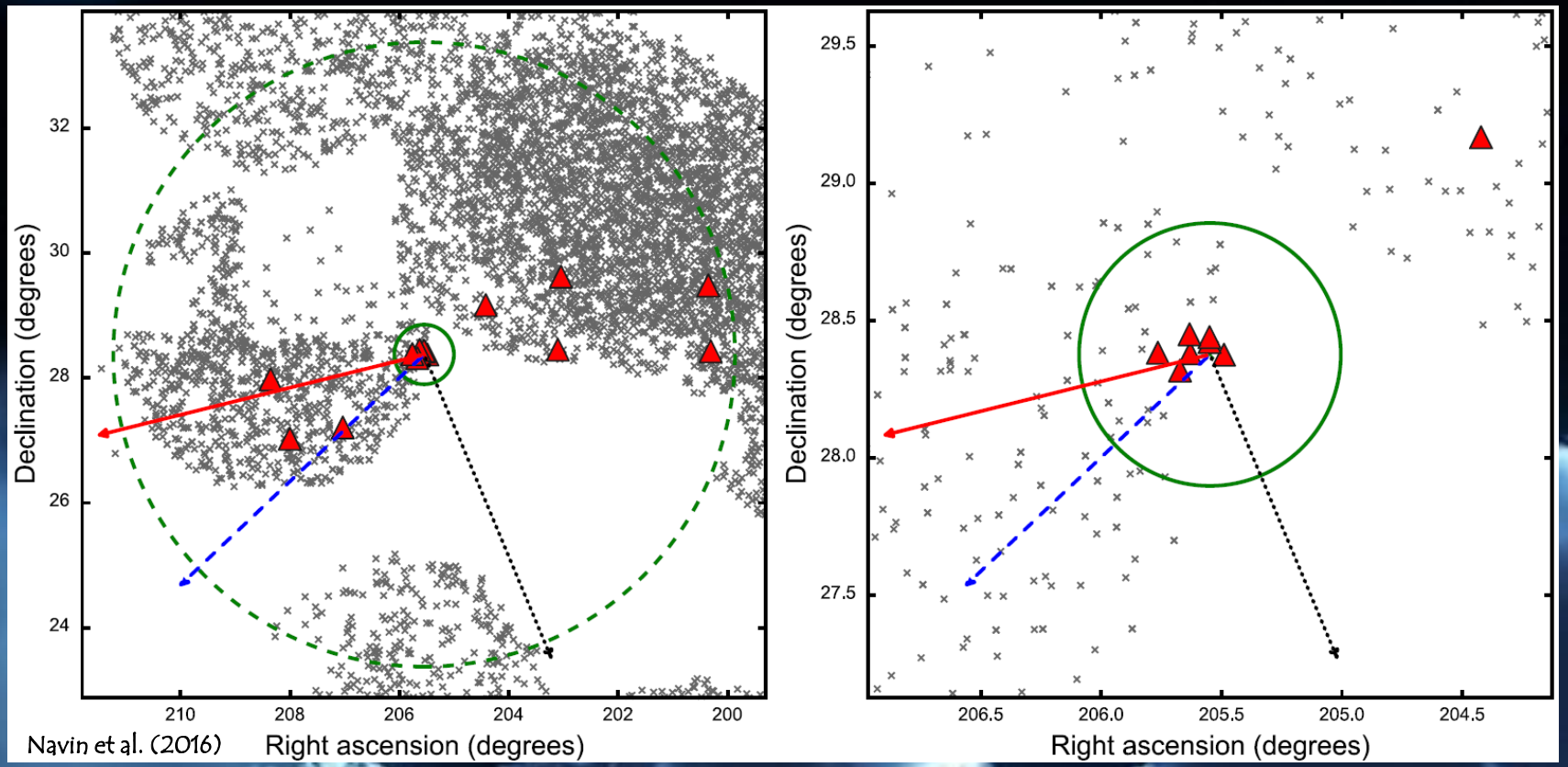

Halo stars of the galactic globular clusters M3 and M13

Left-hand panel: spatial distribution of DR1 Catalog stars around M13. Right-hand panel: expanded version showing the DR1 Catalog stars inside the tidal radius. Gray crosses show non-members, and red triangles denote candidate cluster member stars and candidate extratidal cluster halo stars. The green cross and solid circle show the center position and the tidal radius, respectively; the dashed circle is at a 5° radius from the center position. The black dotted arrow indicates the direction of the cluster proper motion, the blue dashed arrow is the direction to the Galactic center, and the solid red arrow is the direction perpendicular to the Galactic plane.

In this figure there are 12 out of 19 candidate extratidal cluster halo stars.

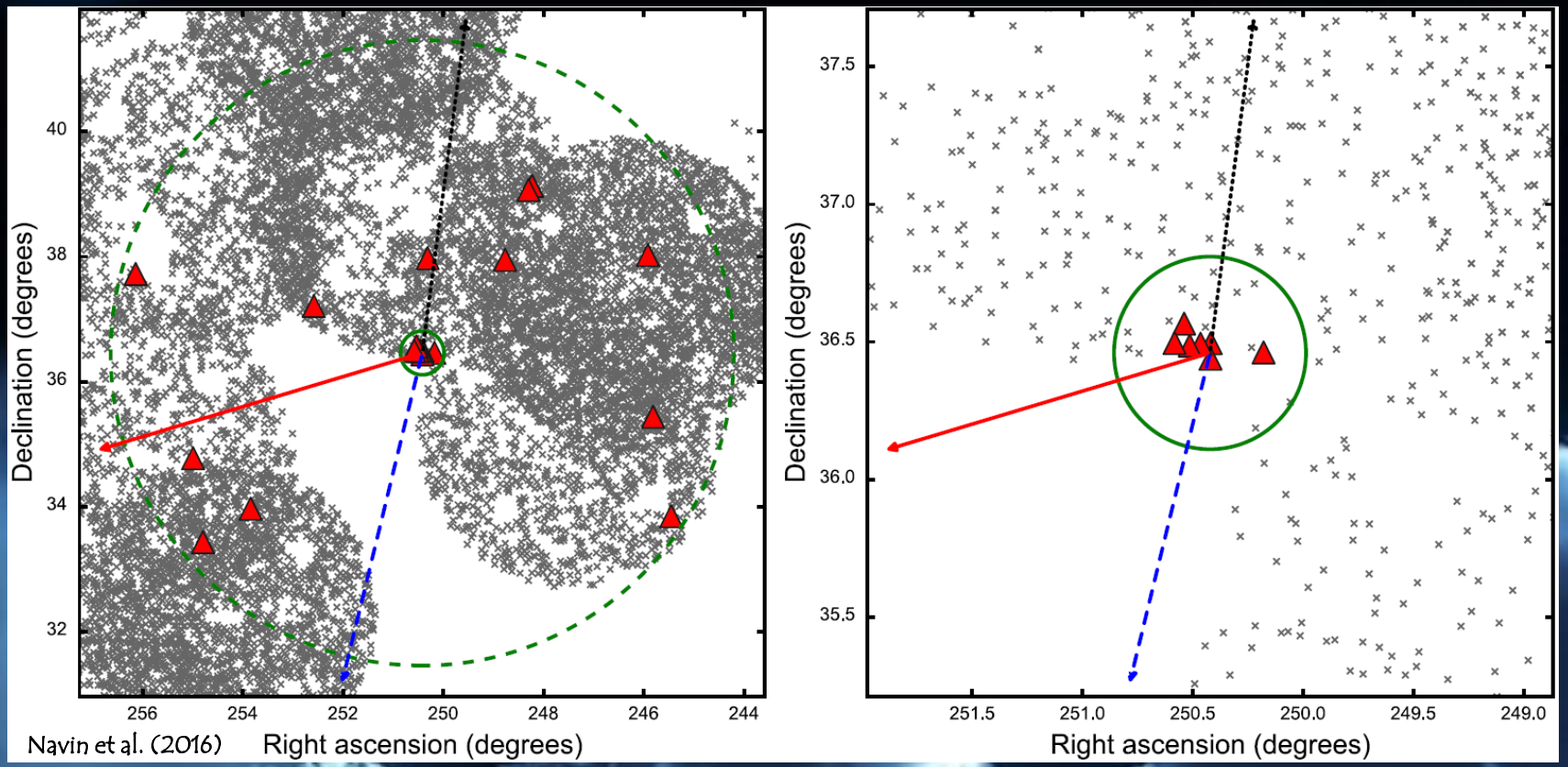

Halo stars of the galactic globular clusters M3 and M13

The globular cluster destruction rates corresponding to the observed mass loss calculated by Navin et al. (2016) are generally significantly higher than theoretical studies predict.

- The estimated destruction rate for M3 is ~1–2 orders of magnitude larger those calculated by Gnedin & Ostriker (1997) and Moreno et al. (2014),
- The estimated destruction rate for M13 is ~1 order of magnitude larger than the destruction rates calculated by Gnedin & Ostriker (1997) but ~3 orders of magnitude larger than those calculated by Moreno et al. (2014).

This visualization presents a globular cluster composed of 6,144 stars. The width of the frame represents more than a hundred trillion miles. As the movie unfolds, the evolution of the cluster is shown in this time-lapse movie, in which each second represents thousands of years passing by. As the stars orbit one other, several stars are ejected from the cluster through close gravitational encounters with more massive stars.

The stars are shown in a scientific approximation of what the human eye would see: each star's brightness depends both on its intrinsic brightness and on its distance away from the virtual camera, while each star's color is only slightly exaggerated.

These calculations were made with the GRAPE-4, one of the fastest special-purpose supercomputers in the world, by Simon Portegies Zwart (University of Amsterdam), Frank Summers (STScI).

Globular clusters in M31 and M33

Bing-Qiu Chen (2015) present a catalog of 908 objects targeted as globular clusters (GCs) and candidates observed with the LAMOST in the vicinity of M31 and M33. The purpose was to to build up a large, systematic spectroscopic dataset for GCs and candidates in this sky area, and to search for new ones.

- 356 of them are likely GCs. The remaining ones are background galaxies , quasars, stars , or H II regions.
- 25 of the GCs are new discoveries.
  - The fall at projected distances ranging from 13 to 265 kpc from M31.
  - One bona fide GC is located near M33 and probably belongs to M33.
  - One bona fide GC falls on the Giant Stream with a projected distance of 78 kpc from M31.
  - One GC has a projected distance of about 265 kpc from M31 and could be an intergalactic cluster.

Table 2 Positions and Properties of Five Confirmed GCs from the SDSS Sample of Targets

Name	RA (deg)	Dec. (deg)	X (kpc)	Y (kpc)	$R_{\rm p}$ (kpc)	$g-r$ (mag)	$r-i$ (mag)	$i_{\rm model}$ (mag)	M_V (mag)	$i_{\rm psf}-i_{\rm model}$ (mag)	$V_{\rm r}$ (km s^{-1})
LAMOST-1	12.23263	35.56682	–49.75	–60.34	78.21	0.77	0.39	17.85	–6.19	1.28	–55
LAMOST-2	24.07521	30.27437	–11.51	–204.43	204.75	0.71	0.33	17.80	–6.18	0.49	–175
LAMOST-3[a]	11.18990	43.44303	26.06	14.11	29.63	0.58	0.28	16.97	–7.05	1.09	–424
LAMOST-4[b]	9.03580	39.29165	–31.37	–2.75	31.49	0.56	0.26	17.12	–6.89	1.18	–230
LAMOST-5[c]	14.73496	42.46061	38.06	–21.18	43.56	0.55	0.27	15.54	–8.44	1.04	–144

[a] Identified previously by Huxor et al. (2014) as 'PAndAS-36' in their Table 1.
[b] Identified previously by di Tullio Zinn & Zinn (2014) as 'D' in their Table 1.
[c] Identified previously by Huxor et al. (2014) as 'PAndAS-46' in their Table 1.

Globular clusters in M31 and M33

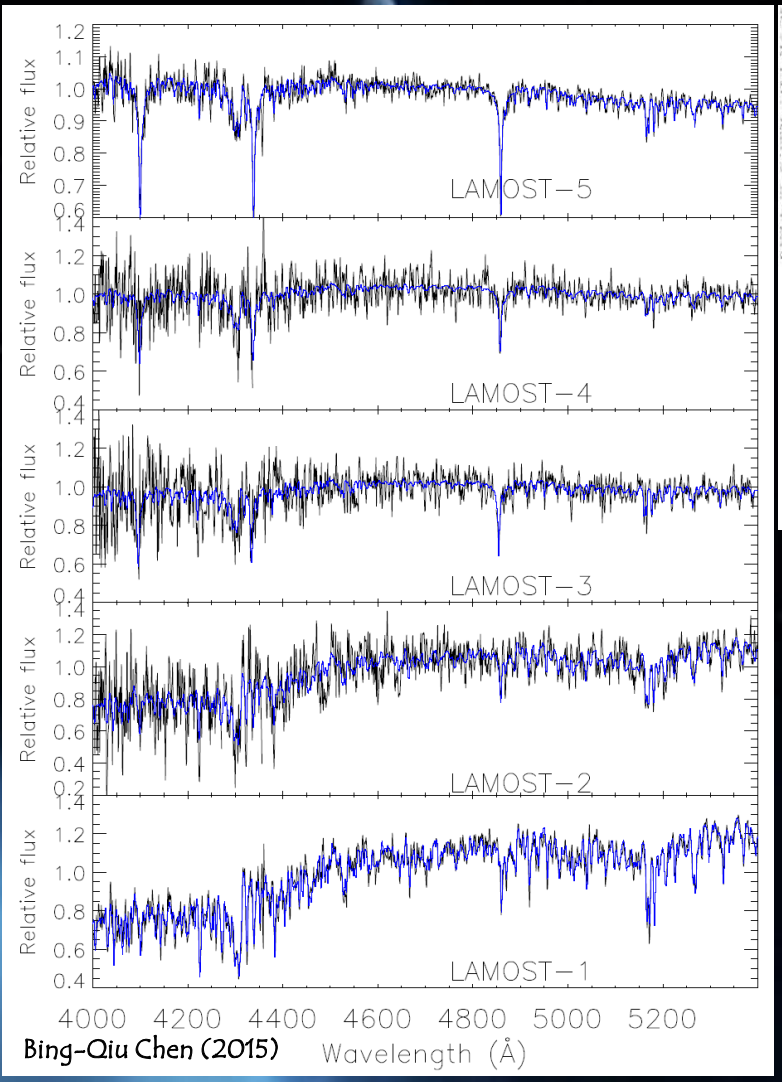

LAMOST spectra of the five new GCs. The observed and model spectra are plotted in black and blue, respectively.

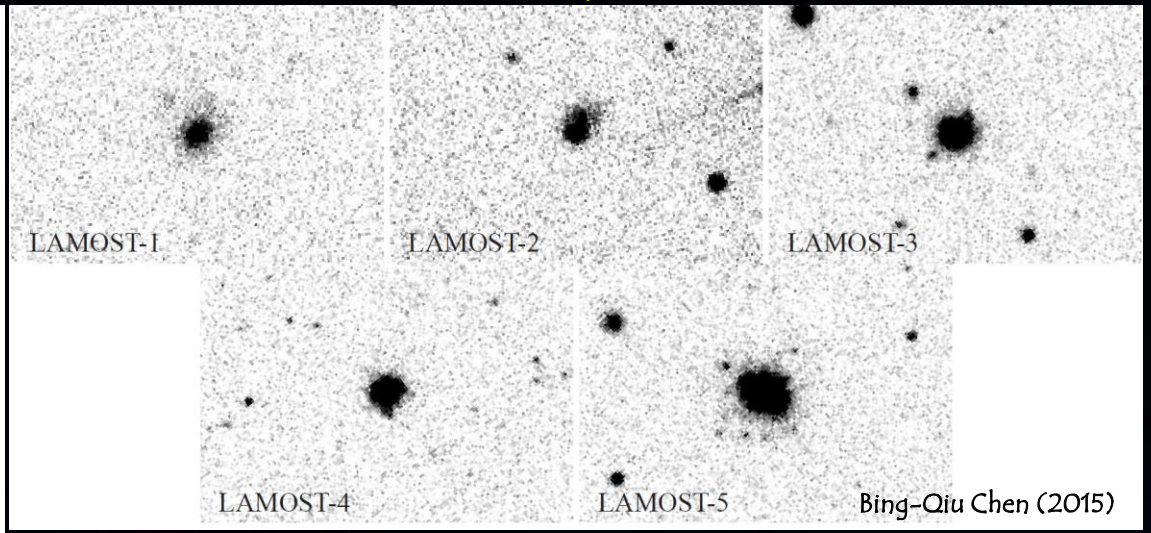

Thumbnails of SDSS r−band images of the five GCs. Each thumbnail is about 1′× 0.7′ in size. North is up and east is to the left.

Globular clusters in M31 and M33

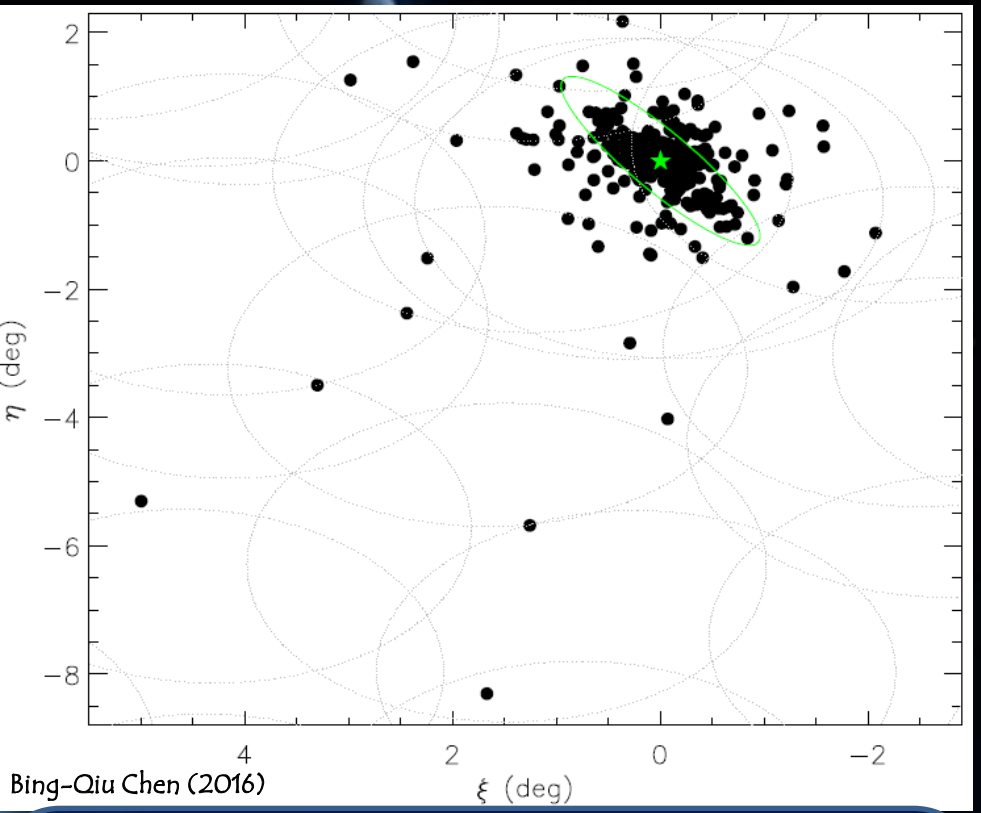

Spatial distribution of the studied sample of star clusters in M31. The large black ellipses show the location of the LAMOST spectroscopic plates observed since June 2014.

The green star marks the central positions of M31.

The green ellipse represents the optical disk of M31 of radius R_{25} = 95.¢3 with an inclination angle i = 77° and a position angle P.A. = 38°.

ξ and η are, respectively, R.A. and decl. offsets relative to the optical center of M31 (R.A.= $00^h42^m44^s.30$; DEC = +41°16′09″)

Bing-Qiu Chen (2016) provides metallicities, ages, and masses for 306 massive star clusters listed by Bing-Qiu Chen (2015).

- Ages range from several million years to the age of the Universe.
- Numbers of clusters younger and older than 1 Gyr are, respectively, 46 and 260.
- A precision of better than 2 Gyr has been achieved for most clusters.
- Metallicities yielded by full spectral fitting have a precision better than ~0.1 dex.
- Cluster masses range from $\sim10^3$ to $\sim10^7$ $M_\odot$, peaking at $\sim10^{4.3}$ and $\sim10^{5.7}$ $M_\odot$ for young (<1 Gyr) and old (>1 Gyr) clusters, respectively.

Globular clusters in M31 and M33

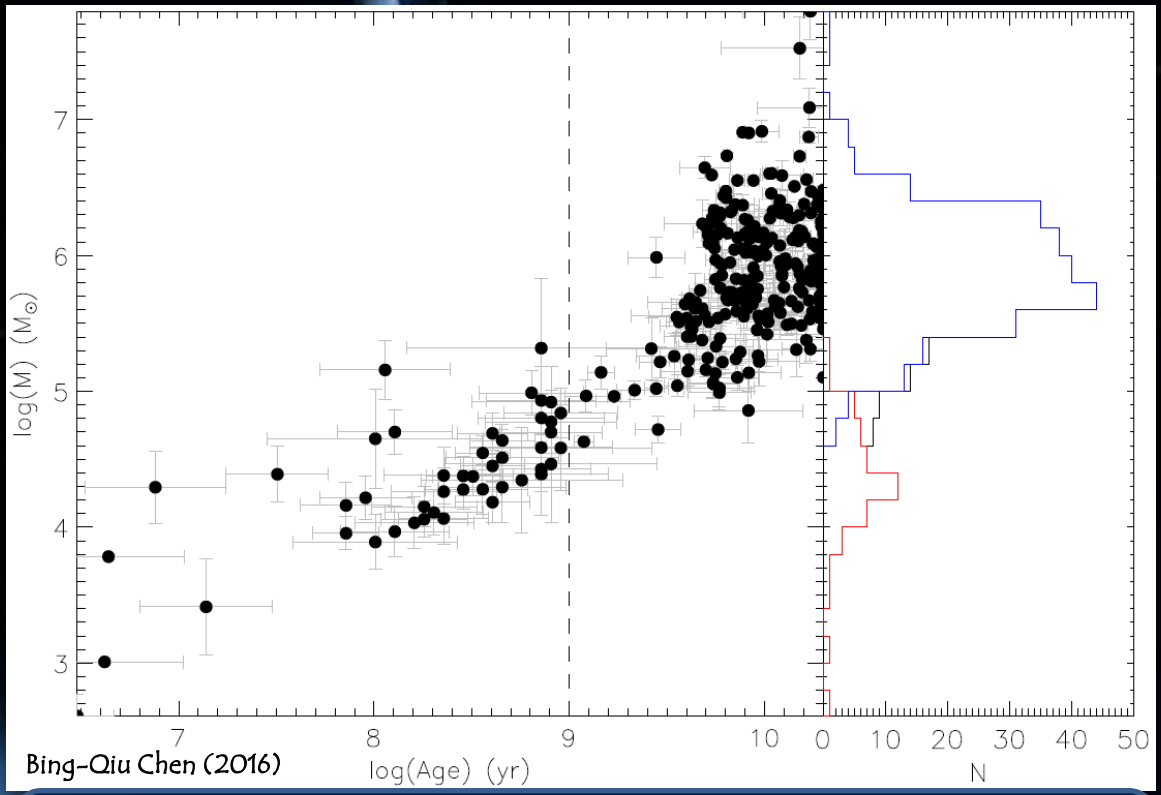

Masses estimated for M31 star clusters v.s. ages of the clusters. The vertical dashed line at age 1 Gyr separates the young and old clusters. A histogram of masses of all clusters is also plotted on the right. Black, red, and green lines give, respectively, the mass distributions of all, young, and old clusters Bing-Qiu Chen (2016).

- The most interesting case is LAMOST-1, a newly identified GC with LAMOST (Bing-Qiu Chen 2015).
- It falls on the Giant Stellar Stream and has a radial velocity suggesting its association with the Stream.
- Bing-Qiu Chen(2016) find a value of metallicity [Fe/H] = −0.4 dex and an age of 9.2 Gyr.
- LAMOST-1 is the most metal-rich among the distant clusters in their sample.
- The metallicity and age derived of LAMOST-1 suggest that it probably formed in an early-type and relatively massive dwarf galaxy, of mass comparable to that of the Large Magellanic Cloud or the Sagittarius (Sgr) dwarf spheroidal.

Globular clusters in M31 and M33

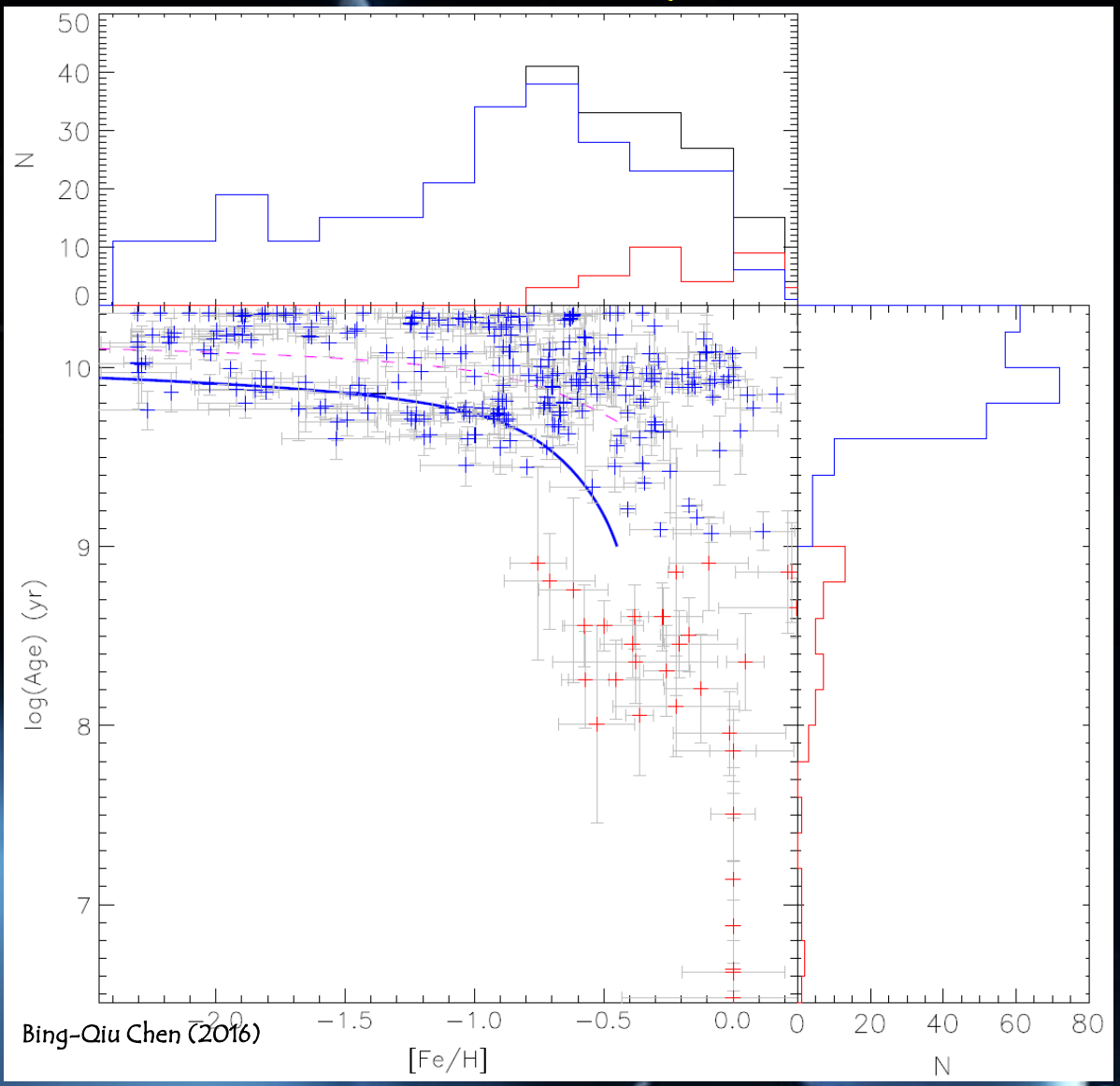

Ages plotted against metallicity for M31 clusters, and the respective histograms: red (46 young clusters) and blue (260 old clusters). The black histogram shows the distribution of all clusters.

The old clusters have a peak at [Fe/H] = −0.7 dex, more metal-rich than the peak value of Galactic GCs. Young clusters have metallicities comparable to the Sun

The pink dashed line delineates age-metallicity relation of (accreted) Galactic GCs associated with the Sgr and CMa dwarf galaxies from Forbes & Bridges (2010). The blue line is the same relation but shifted by 4 Gyr. Bing-Qiu Chen (2016).

Globular clusters in M31 and M33

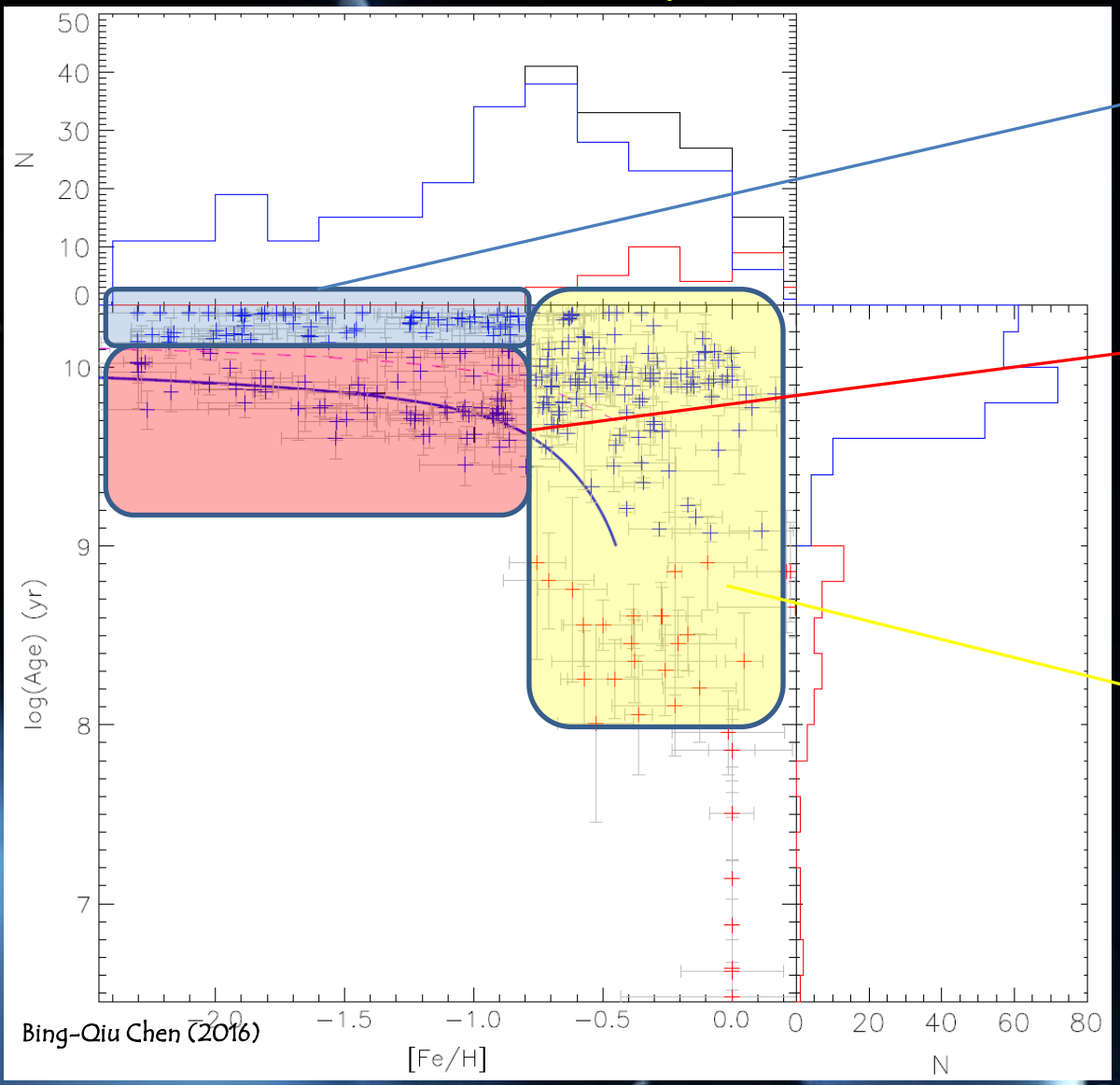

This group has the oldest ages and metallicities poorer than ~ -0.7 dex, with no age–metallicity relation. They were probably formed in situ in the halo in the early epoch of M31 with a rapid process.

This group has metallicities poorer than ~−0.7 dex but shows a clear age–metallicity relation, The young clusters are more metal-rich than the old ones. They probably come from disrupted dwarf galaxies accreted by M31 in the past. M31 may have been subjected to substantial merger events more recently than the MW.

This group has metallicities richer than ~-0.7 dex and spans a wide range of ages. A significant fraction of them have ages about 8–9 Gyr and are mainly found in the disk of M31. These clusters might also form in situ in the disk of M31, but at an epoch much later than those formed in the halo.

Stellar intrinsic colors in the infrared

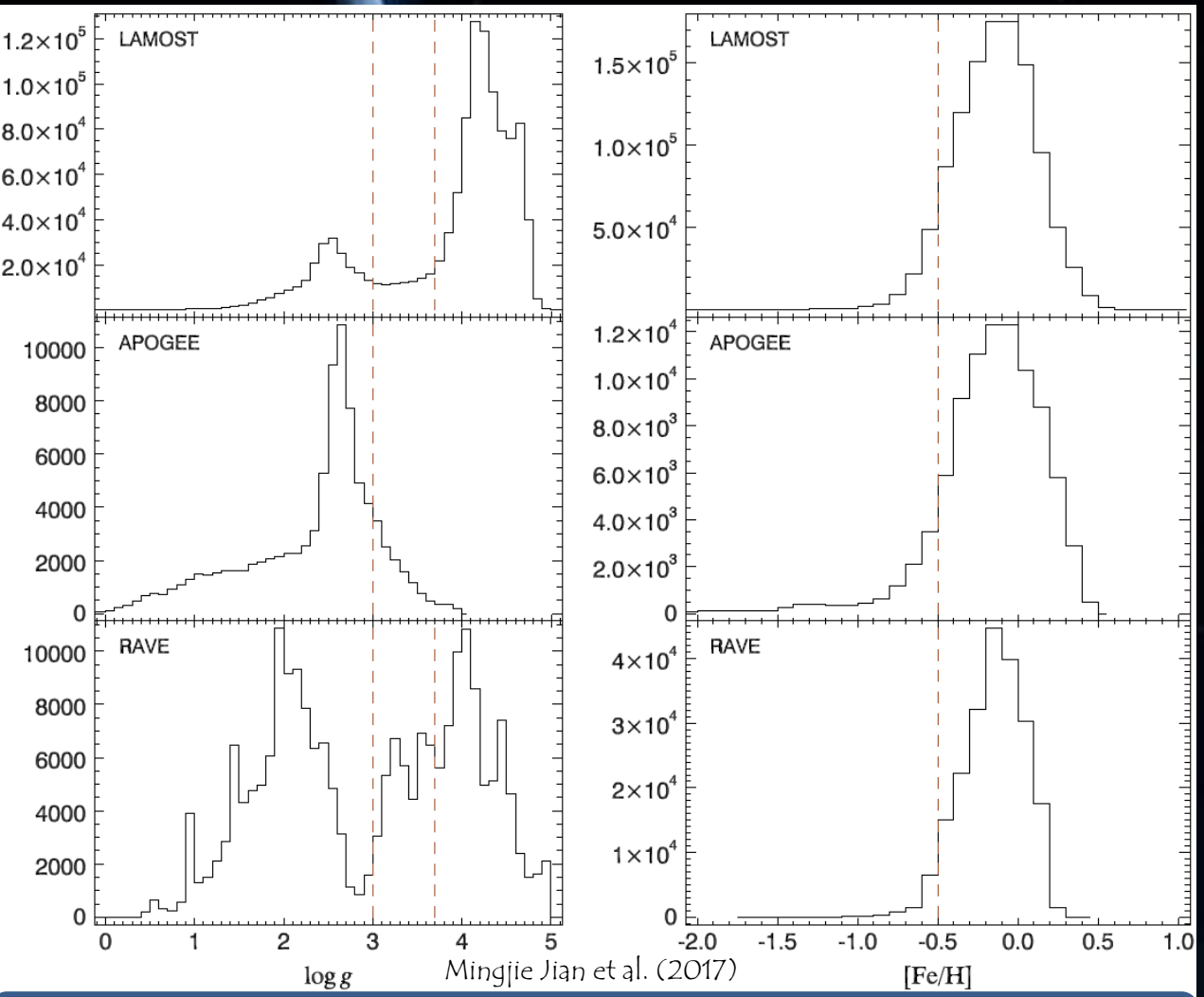

Distribution of log *g* and [Fe/H] from spectroscopic surveys. Brown dashed lines are borders used to separate dwarf and giant stars. The LAMOST sample is the largest.

Stellar intrinsic color (the color index) is a fundamental parameter associated with the properties of the stellar atmosphere. The color indices reveal the information about spectral energy distribution and can be used to estimate the extinction law.

Due to numerous molecular absorption bands in the infrared, theoretical determination of stellar color indexes suffers different uncertainties. Therefore, Mingjie Jian et al. (2017) derived the color indices in the popularly used infrared bands used by the Two Micron All-Sky Survey/JHKS, Wide-field Infrared Survey Explorer, Spitzer/IRAC, and AKARI/S9W filters based on spectroscopic surveys by LAMOST, RAVE, and APOGEE.

Stellar intrinsic colors in the infrared

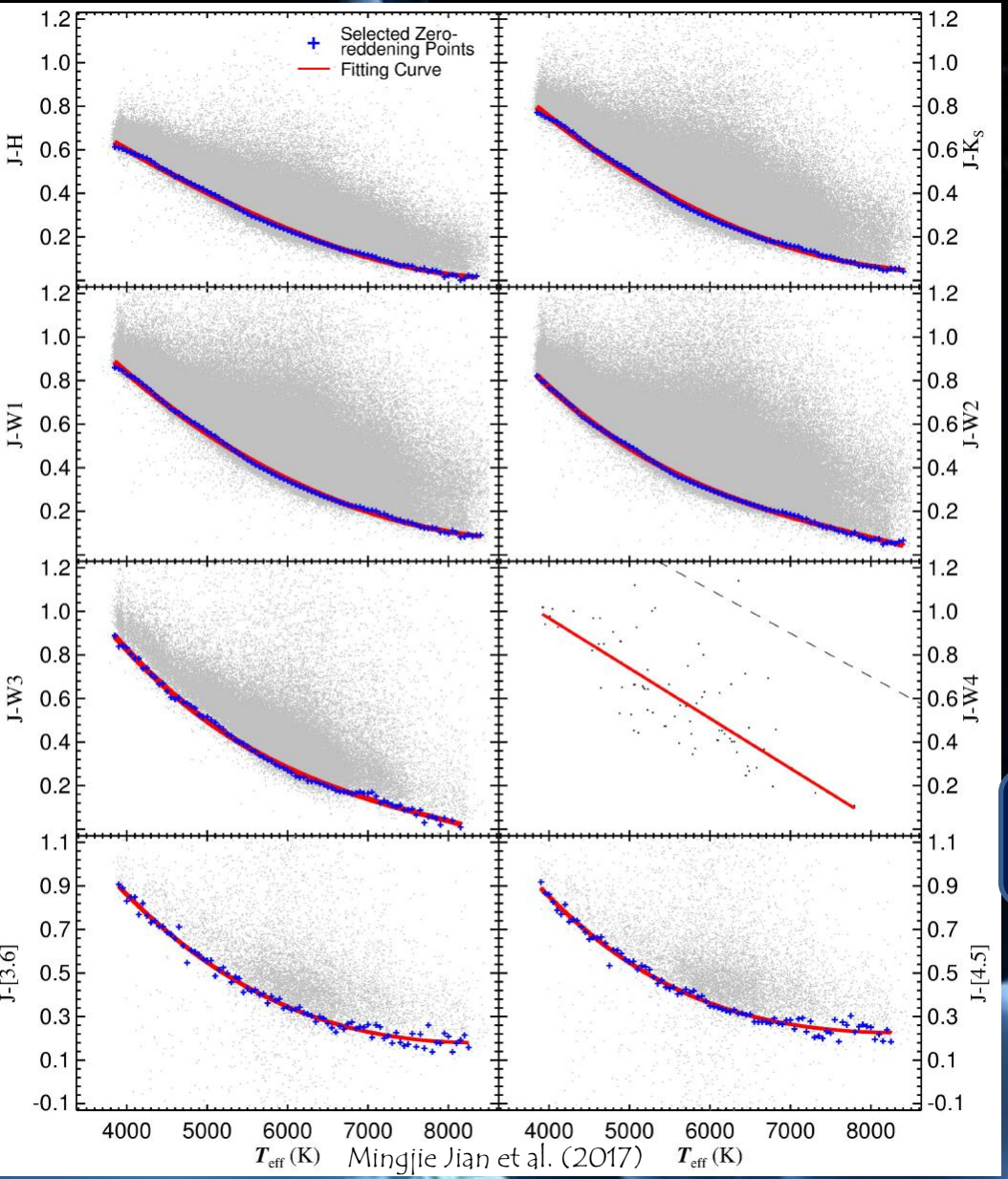

Left: Color–T_{eff} diagrams of dwarf stars from the LAMOST survey. Gray/black points indicate stars that passed data quality control, blue crosses indicate the selected zero-reddening stars. The red line is the fitting curve. The stars under the dashed line in the $J - W_4$ diagram is adopted for a linear fitting.

To determine the intrinsic color indexes, Mingjie Jian et al. (2017) used the method of Ducati et al. (2001) assuming that the bluest star for a given spectral type has the smallest interstellar extinction. If the sample includes stars with no interstellar extinction, the observed color of the bluest star is equivalent to the intrinsic color of the given type.

With these discrete intrinsic color indexes determined, a third-order polynomial function of the intrinsic color index ($C_{\lambda1\lambda2}^{0}$) between bands $\lambda1$ and $\lambda2$ is fitted to the effective temperature (T_{eff}):

$$C_{\lambda1\lambda2}^{0} = a0 + a_1 T_{eff} + a_2 T_{eff}^{2} + a_3 T_{eff}^{3}$$

The result from LAMOST is recommended for the dwarf stars, because APOGEE lacks a good sample of dwarfs and RAVE covers a smaller range of T_{eff} than LAMOST.

Active stars

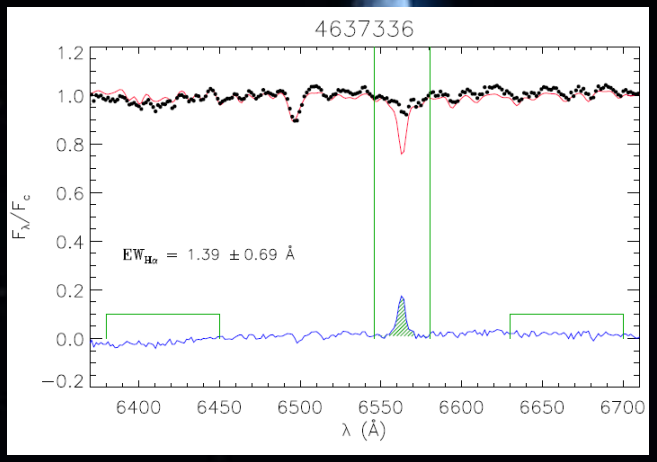

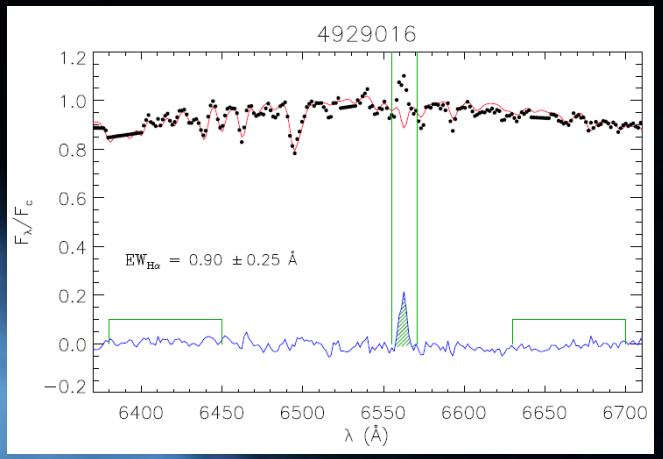

Frasca et al. (2016)

LAMOST-Kepler project: round 1

- Detection of 547 stars which show Hα in mission or filled in,
- 442 GKM stars classified as chromospherically active from the flux–flux relationship between Hα and Ca II IRT,
- Discovery of an accretting star KIC 8749284 (K1 V).

Boundary between chromospheric emission (below the line) and accretion as derived by Frasca et al. (2015).

KIC 8749284 (K1 V) – the only star in the domain of accerting objects.

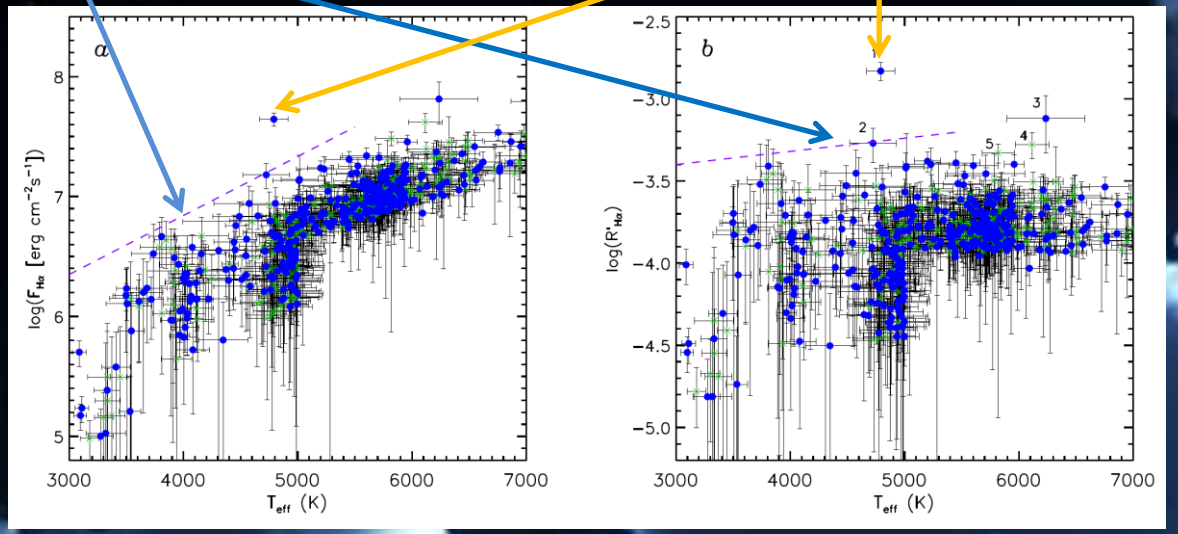

Active stars

Talks by
Yuta Notsu,
Li-Ching Huang

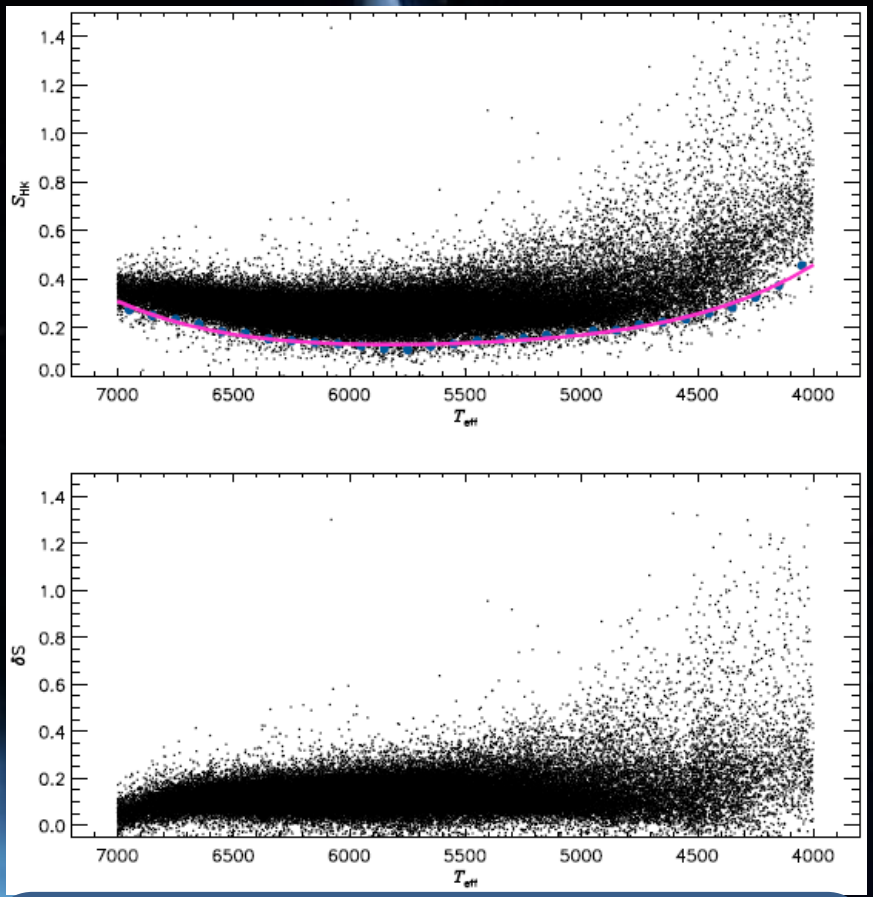

The index δS for each of these stars is calculated by the difference between its S_{HK} value and the baseline determined from very inactive stars. The blue filled circles represent the most inactive 5% of stars in each bin. The magenta line is the baseline for "inactive stars" by fitting these points with a fourth order polynomial. *Bottom*: δS vs. Teff for the sample analysed by Jing-Kun Zhao et al. 2015.

Measurements of the chromospheric activity index S_{HK} (the ratio of the flux in the core of the Ca II H&K lines to the nearby continuum) for 119,995 F, G and K stars from LAMOST DR1 has been carried out with the aim of investigating the chromospheric activity distribution as a function of T_{eff}, [Fe/H] and kinematics by Jing-Kun Zhao et al. 2015.

CaII H&K emission is a useful marker of the chromospheric activity in lower main sequence stars. That activity is widely used as an age indicator for solar-type stars. In late F to early M stars, the CaII H&K emission, magnetic field strength and rotation all decay as the inverse square root of stellar age. However, the viability of this age indicator can be limited to stars younger than about 1.5 Gyr (Pace et al. 2009; Pace 2013).

Active stars

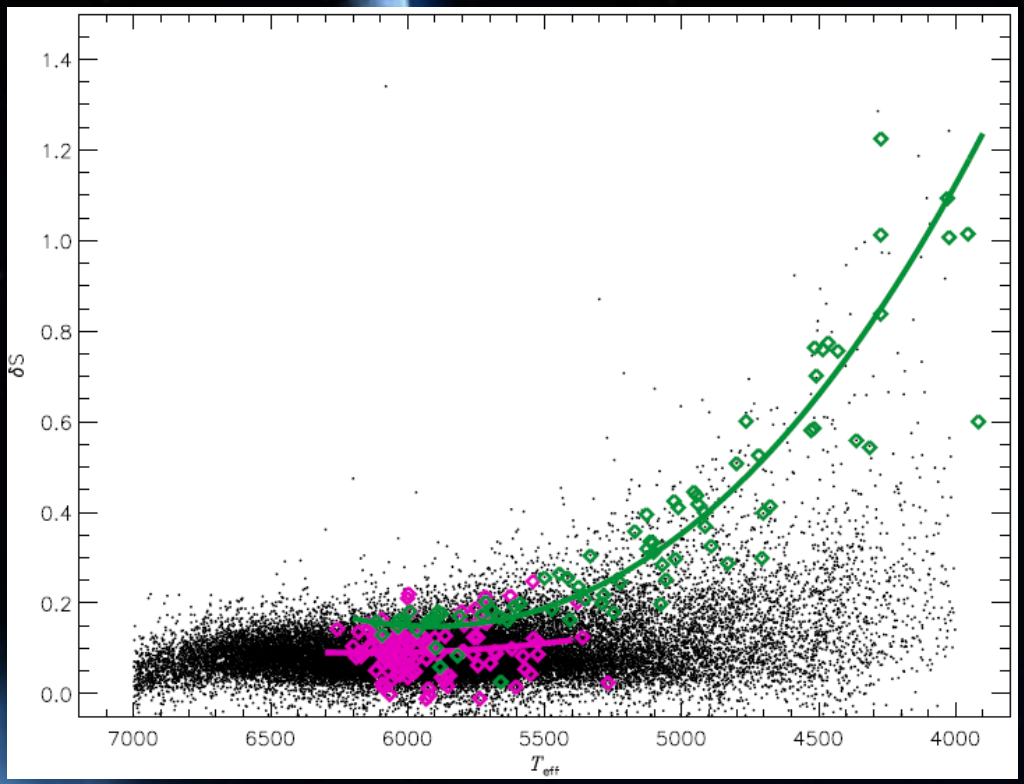

The δS distribution of the sample analyzed by Jing-Kun Zhao et al. overplotted by δS measured in two open clusters M45 (Pleiades, age of ~130 Myr) and M67 (age ~ 4.05 Gyr). Green diamonds represent the member stars of M45. The solid green line is the least squares fit with a fourth order polynomial. The red diamonds are the member stars of M67 and the red solid line is a similar fit for M67 (Jing-Kun Zhao et al. 2015).

Results of the analysis of LAMOST DR1 stars:

- No evident relation between chromospheric activity and metallicity among G stars.
- Some F stars seem to have stronger chromospheric activity, perhaps because of their lower metallicity.
- Only stars with T_{eff} < 5500 K show a correlation with Z. Active stars lie closer to the Galactic plane and they tend to have relatively smaller UVW velocity.
- In two open clusters, M45 and M67, young stars and old stars can be statistically discerned by using chromospheric activity.

Active stars: spots on 304 Pleiades candidate members

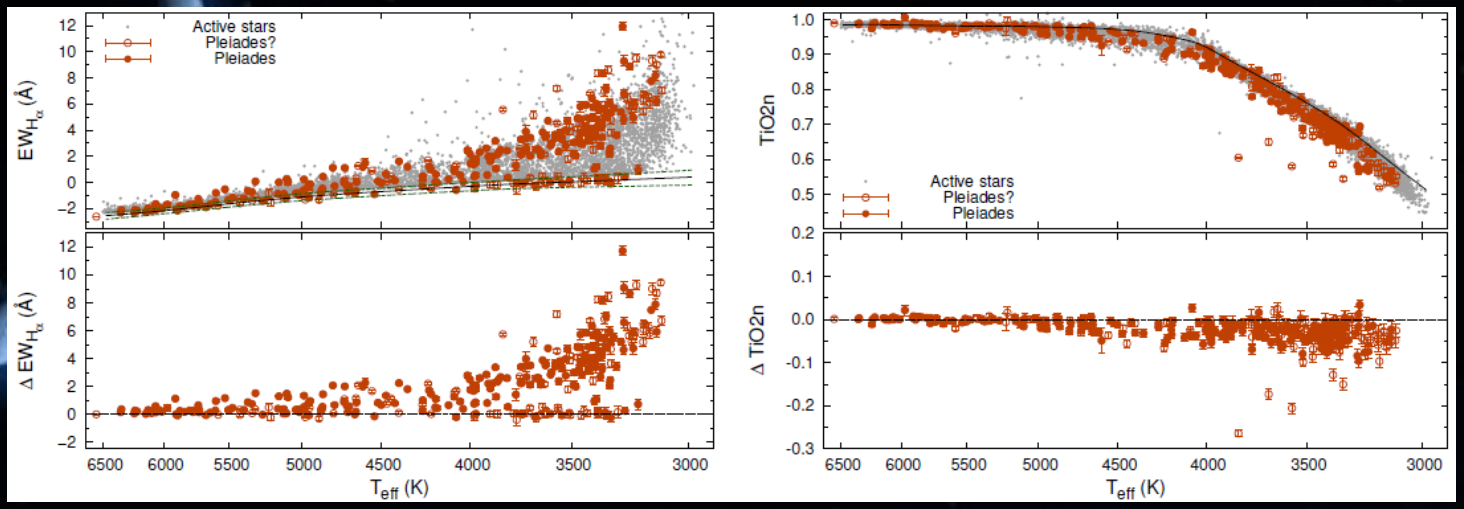

Measurements of $EW_{H\alpha}$ and TiO2n and their corresponding deviations ($\Delta EW_{H\alpha}$ and ΔTiO_2n) to the mean values for entire sample stars are shown in left and right panel, respectively. Black solid lines show the mean relations for inactive counterparts. In the upper left panel, upper 3.5σ and lower 4σ to mean $EW_{H\alpha}$ are shown in green dashed lines (Xiang-Song Fang et al. 2016).

- $EW_{H\alpha}$ measured for the Pleiades members indicate that they are chromospherically active.
- The ΔTiO_2n measurements show that the active stars and Pleiades candidate members are found to have deeper TiO2 absorption compare to their inactive counterparts, indicating the presence of cool spots.
- TiO absorption features appear in the spectra of active stars, even hotter stars like G- and early K-type stars, indicating the presence of cool star spots on their photospheres.
- The spot coverage of G-type members are generally less than 30%, while a large fraction of K- and M-type members appear to be covered by very large cool spots with filling factors over the range of 30%–50%.
- Faster rotating G- and K-type stars are covered by larger spots.
- Large spot coverages has been detected in many M type members showing no or little light variation.

Flaring M-type dwarfs in the Kepler field

Stellar flares are explosive events because of the sudden release of a large amount of energy in a short time interval.

M dwarfs (dM stars) are known to have frequent flares, (especially the late-type M stars, i.e., M3–M9).

- Scientific interests:
  - it is still uncertain whether the generation mechanism is similar to that of solar flares
  - relevant to the issue of exoplanetary habitability
- Difficulties: limitations in time coverage and sample.
- Remedy: long time-series obtained with the Kepler satellite

Classification of flares on dM stars:

- simple flares, characterized by a single peak; the time evolution of single-peak events can be further divided into three phases:
  - impulsive rise
  - impulsive decay
  - and gradual decay
- complex flares, with multiple peaks.

This morphology is typical to solar flares, which are generated by the conversion of magnetic energy to plasma kinetic energy. That means that the flare activity of dM stars can be correlated with the level of chromospheric emission.

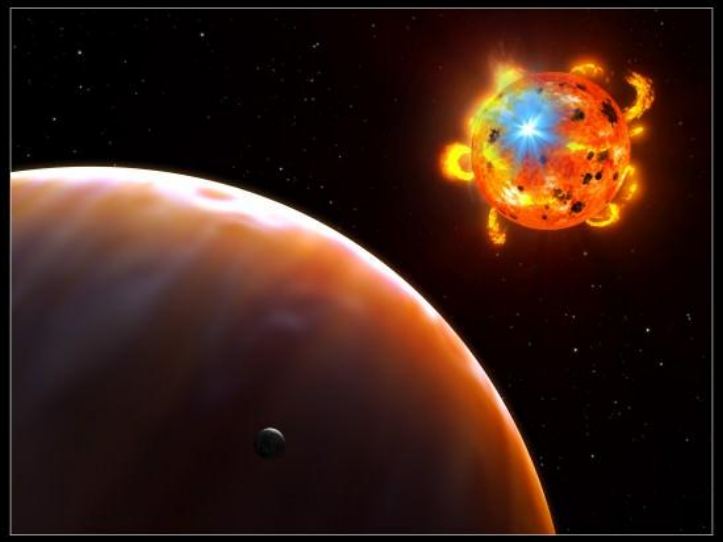

Artist's View of Dwarf Flare Star

NASA, ESA, and G. Bacon (STScI) • STScI-PRC11-02

Do dM stars with high Hα emission brightness produce strong flare activity?

Flaring M-type dwarfs in the Kepler field

H.-Y. Chang et al. (2017) identified 54 M0–M3 dwarfs which have the Kepler light curves and have been the LAMOST dM star targets.

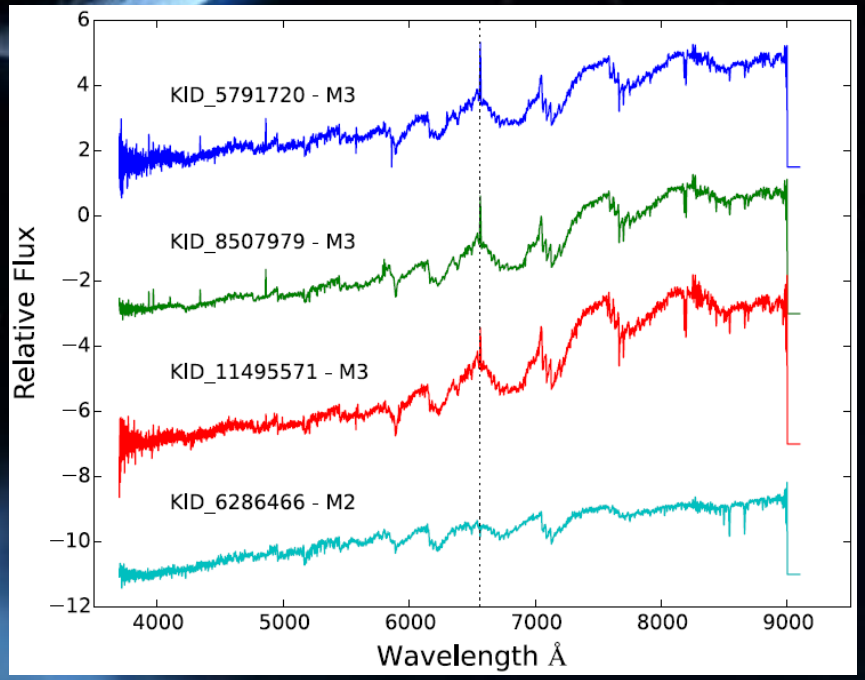

The LAMOST spectra of four M dwarfs observed by Kepler. The Hα line at 6562.8 Å is indicated with the vertical line. KIC5791720 and KIC8507979 show emission in the lines Hβ at 4861 Å and Hγ at 4341 Å can be clearly identified (H.-Y. Chang et al. 2017).

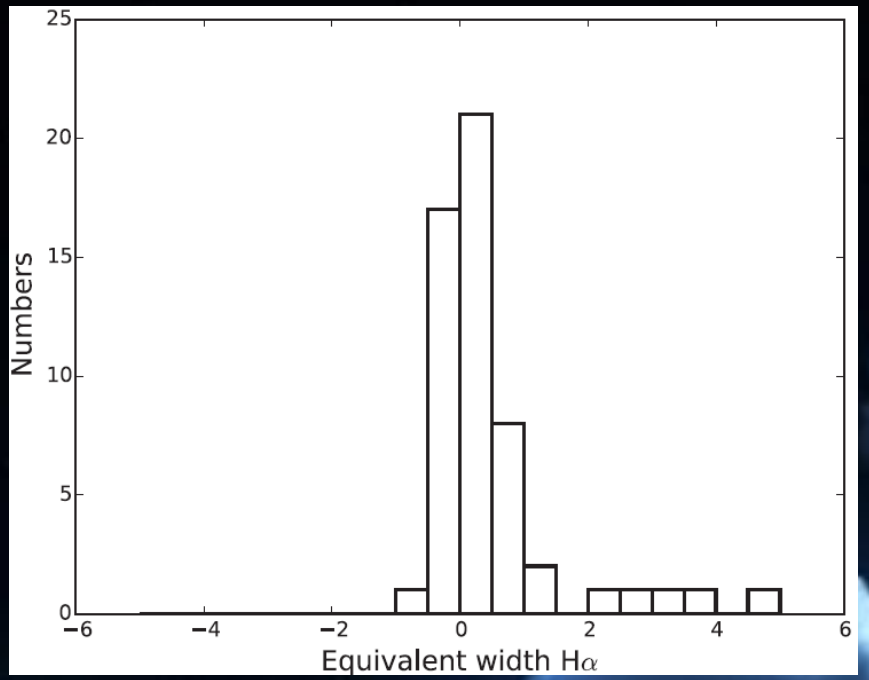

A histogram of the number distribution of the 54 M dwarfs as a function of Hα EW. The emission EW has a positive value, and the absorption EW has a negative value (H.-Y. Chang et al. 2017).

Flaring M-type dwarfs in the Kepler field

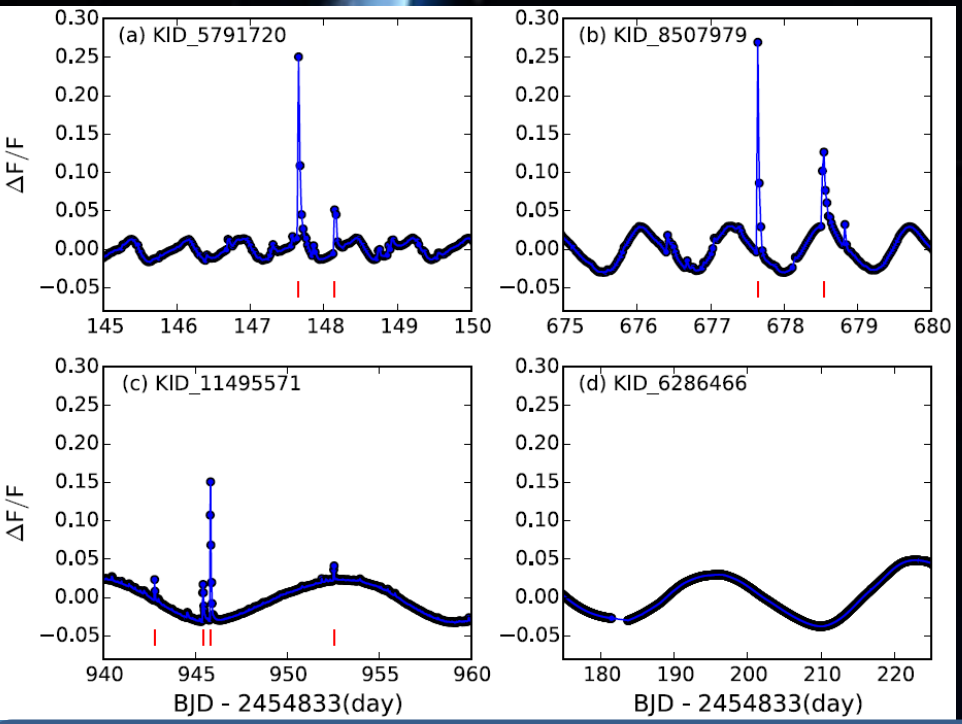

The light curves of four dM stars. Flares can be found at different phases of the periodic modulations of the light curves produced by star spots (H.-Y. Chang et al. 2017).

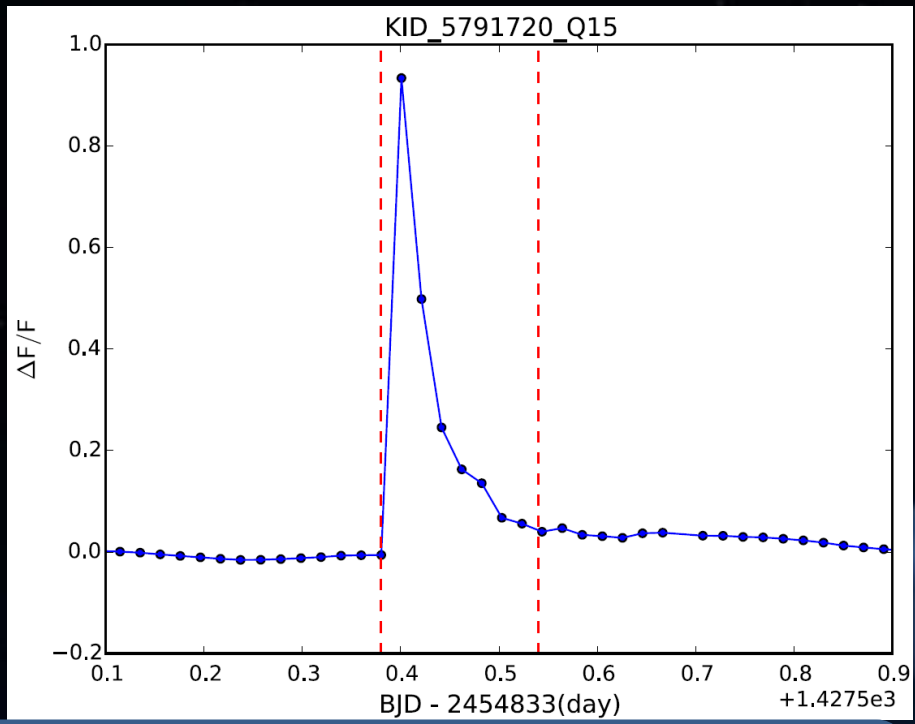

A time profile of a super- (or hyper-) flare of KIC 5791720 with the peak flux reaching almost the same level as the stellar luminosity of this M3 star. The two red dashed lines indicate the time interval for the flare energy calculation (H.-Y. Chang et al. 2017).

Flaring M-type dwarfs in the Kepler field

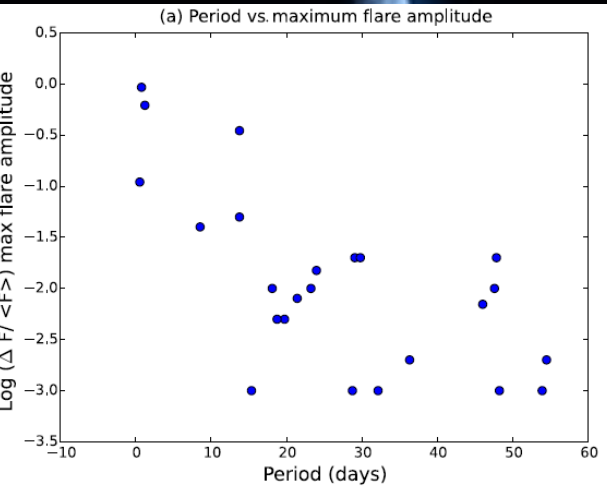

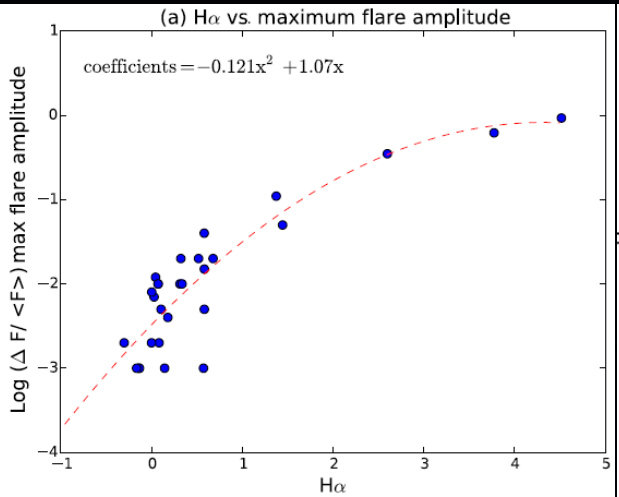

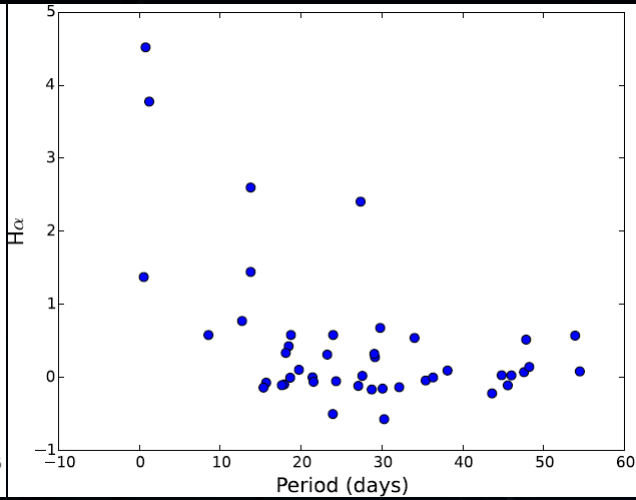

H.-Y. Chang et al. (2017)

- There is an apparent cutoff at P~20 days for flares with large amplitude (>3%) to appear.
- M dwarfs with strong chromospheric emission in Hα have large flare activity.
- A higher magnetic activity is detected in faster-rotating M dwarfs (rotation periods < 20 days).

Superflares on solar-type stars

- Superflares are defined as flares with energies ranging from 10^{33} to 10^{38} erg.
- *Kepler* observations: 365 superflares on 148 solar-type stars (Maehara et al. 2012) and 1,547 superflares on 279 G-type stars (Shibayama et al. 2013).
- Karoff et al. (2016) used LAMOST to show that superflare stars are generally characterized by larger chromospheric emissions than other stars, including the Sun.

Superflares on solar-type stars

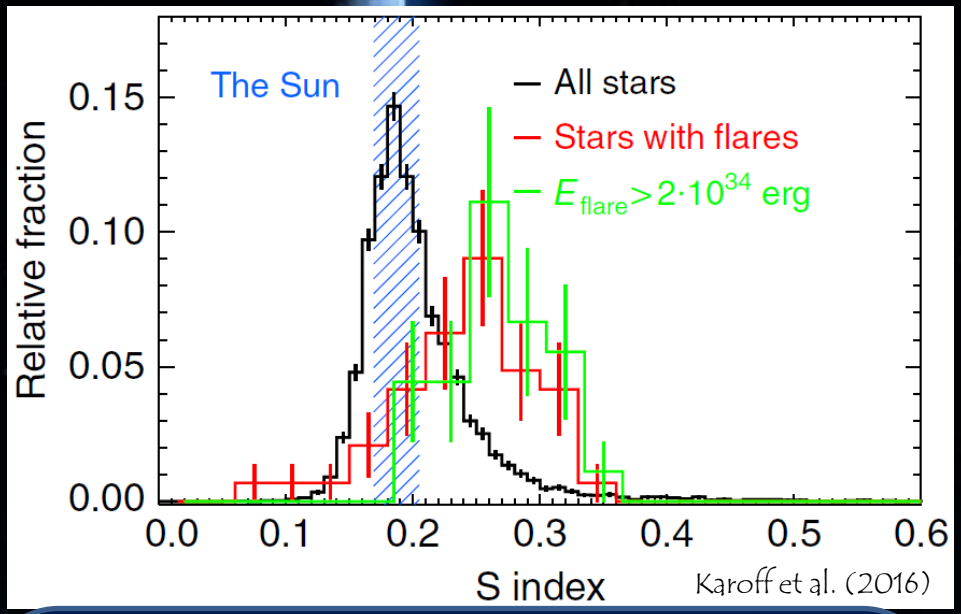

Histograms of the activity distribution of solar-like stars (main-sequence stars with T_{eff} between 5,100 and 6,000 K) in black compared with those of these stars that show superflares in their Kepler light-curve in red.

The blue shaded region marks the range of the S index of the Sun between solar cycle minima and maxima.

The two distributions are different at a 6σ level, clearly showing that the superflare stars generally have higher activity levels than average solar-like stars. The green curve shows the distribution of superflare stars with total energies larger than $2\cdot10^{34}$ erg.

Superflares on solar-like stars may result from at least three different mechanisms apart from coronal magnetic reconnection:

- star–star interactions (a RS CVn-type star–star interaction is unlikely)
- star–disk interactions (difficult to evaluate),
- star–planet interactions (none of the superflare stars are known to host hot Jupiters)

The study of Karoff et al. (2016) provides observational support for the coronal magnetic reconnection hypothesis. The coronal magnetic reconnection hypothesis can explain the observations via the notion that superflares and solar flares share the same origin.

Superflares mainly take place on stars with activity levels larger than the Sun.

- 1,150 out of 1,547 superflares occurred on fast rotating stars (Shibayama et al. 2013).
- Studies of ^{14}C in Japanese tree rings indicate that the Sun hosted a superflare with an energy larger than 10^{33} erg in AD 775 and AD 993 (Miyake et al. 2012, 2013).

Solar superflares in 775 and 994?

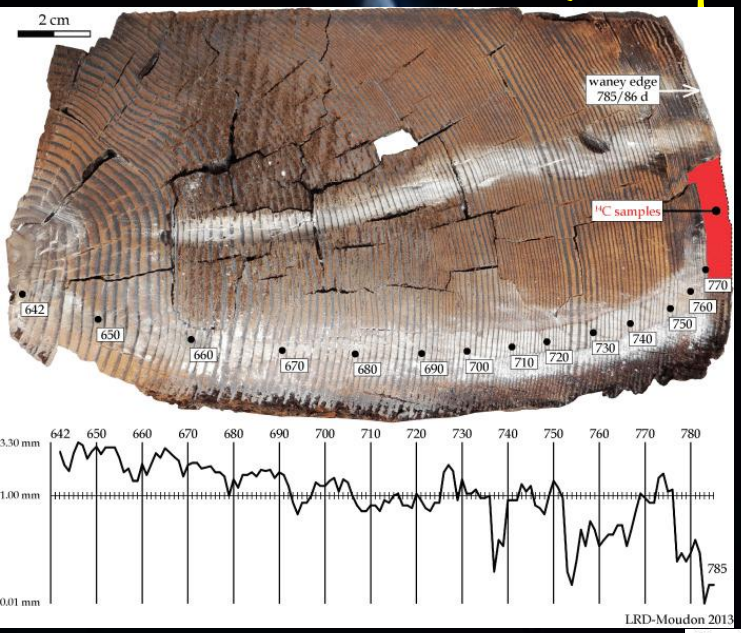

Timber from the Holy Cross chapel of the convent St. John the Baptist in Val Müstair, Switzerland (Wacker et al. 2014).

Radiocarbon ^{14}C is produced in the Earth's atmosphere by nuclear interactions with galactic cosmic rays, most of which are charged particles. The flux of cosmic rays is modulated by the solar magnetic activity and the geomagnetic field.

Radiocarbon oxidizes in the atmosphere to form $^{14}CO_2$ and is taken up by trees as a part of the global carbon cycle.

As ^{14}C is a radioisotope with a half-life of 5,730 years, the ^{14}C content in tree rings provides a record of cosmic ray intensity and solar activity over a few tens of millennia.

The large solar proton events can produce a large number of cosmic rays all at once. Then, if such events have occurred in the past, the ^{14}C content in tree rings is possible to record the rapid increase due to the events. (from Miyake et al. 2013).

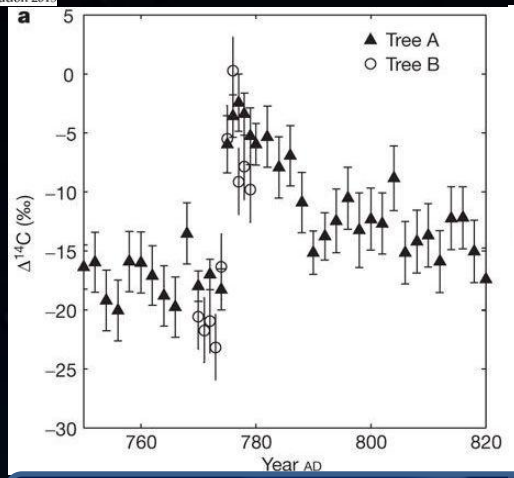

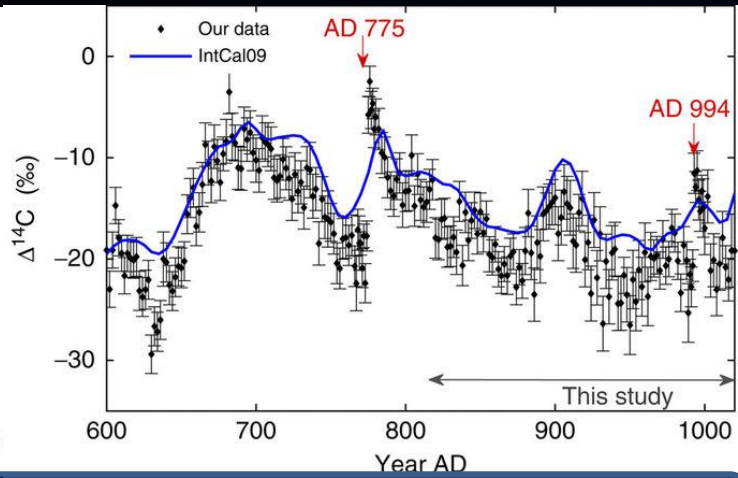

The concentration of ^{14}C is expressed as $\Delta^{14}C$, which is the deviation (in ‰) of the $^{14}C/^{12}C$ ratio of a sample with respect to modern carbon (Miyake et al. 2012, 2013).

Emission-line stars

A catalogue of early-type emission-line stars and Hα line profiles (Wen Hou et al. 2016, RAA, 16, 138).

11,204 spectra for 10,436 early-type emission-line stars from LAMOST DR2 (9,752 new discoveries)

The spatial distribution of the sample observed with LAMOST. The blue and red points represent 200,000 O, B, A stars and 11,204 early-type H emission-line stars respectively. These two samples are concentrated in the region of Galactic Anti-centre due to the observational strategy. The cyan boxes represent HII regions.

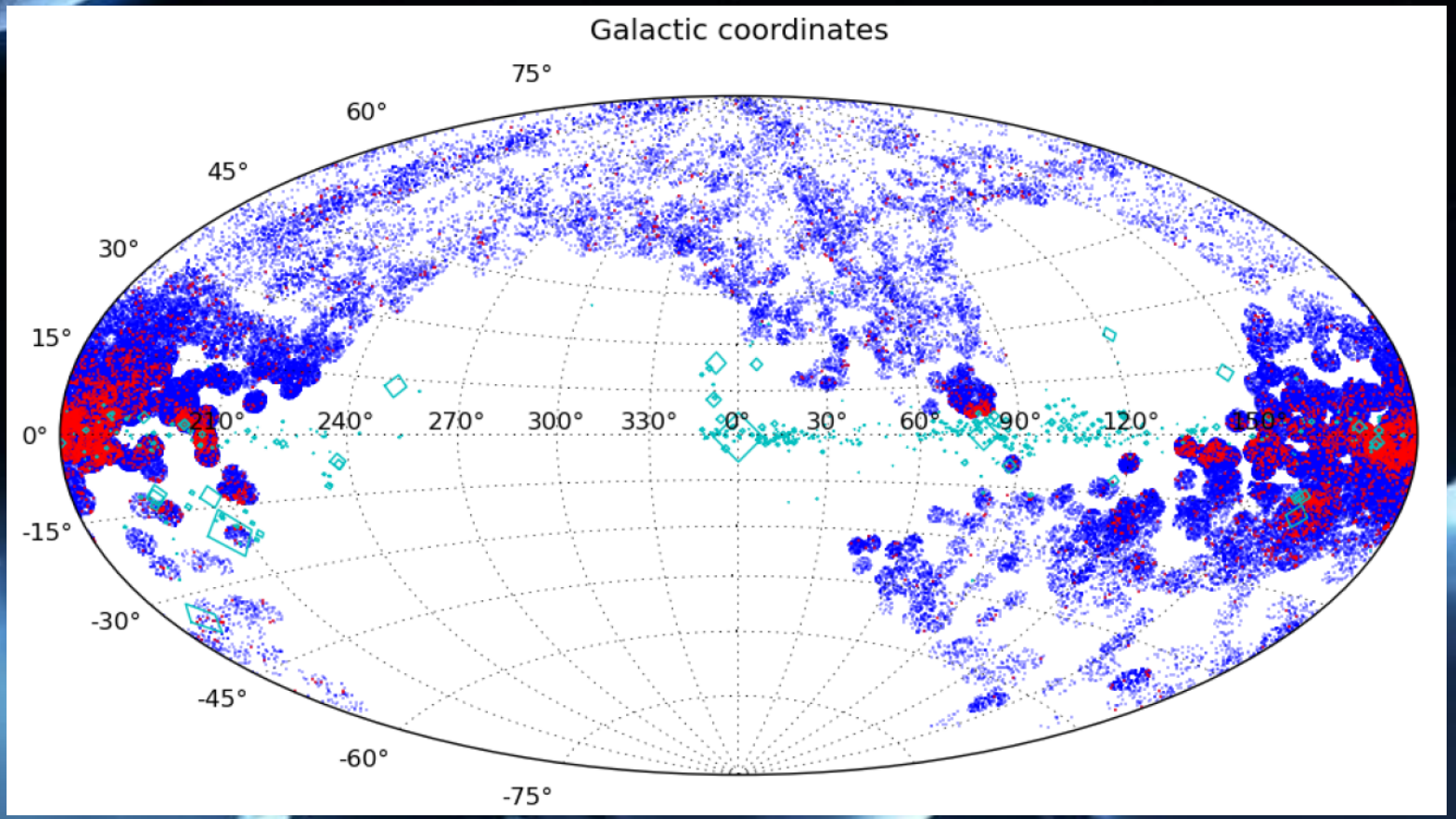

Emission-line stars

172 spectraof stars showing Fe II emission lines (Wen Hou et al. 2016, RAA, 16, 138).

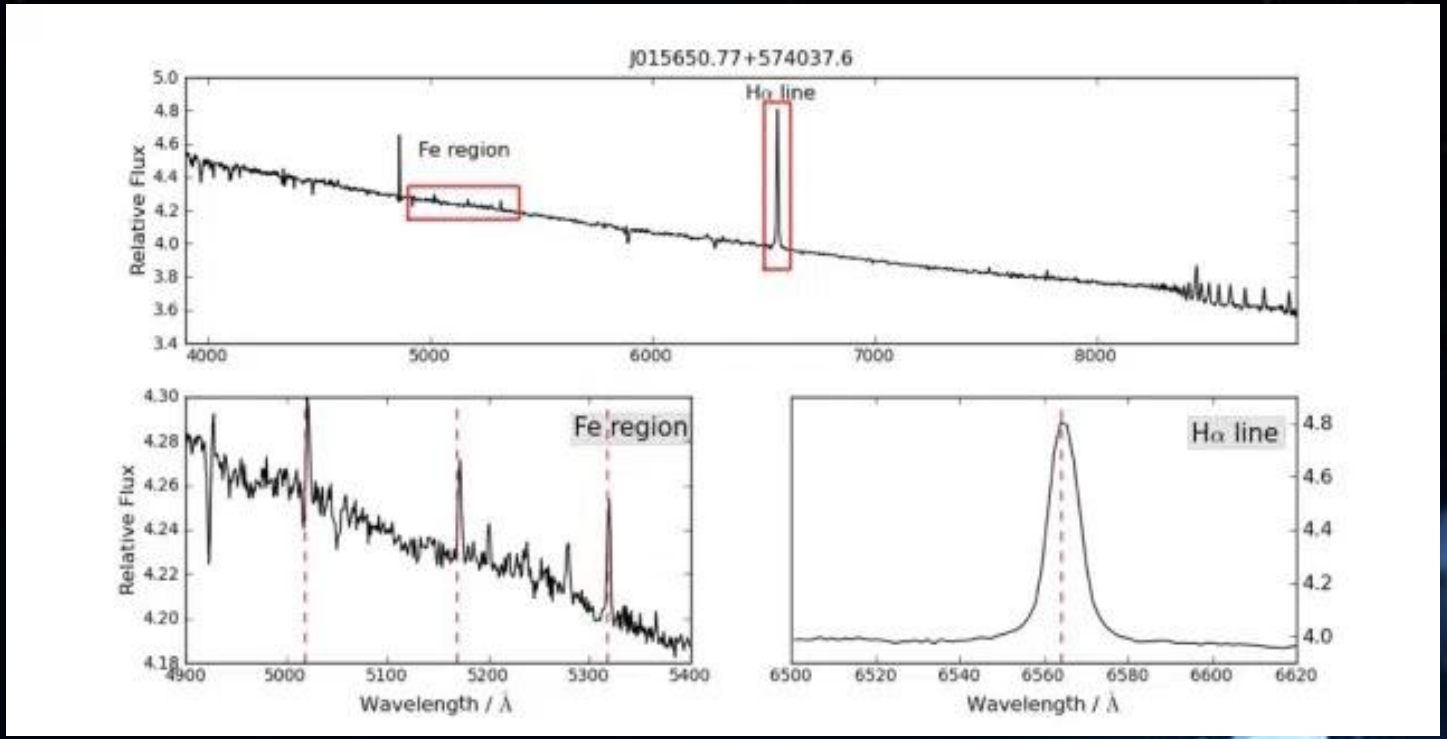

Fe II emission lines with single-peak. The spectrum of wavelength ranging from 3800 Å to 8900 Å is plotted in the top panel. Two regions of the spectrum are shown in the bottom, which are the features of Hα profile and iron lines respectively. Three lines of Fe II 5018 Å, 5169 Å, and 5317 Å used in the emission detection are marked by the red dotted line in the left-bottom panel. (Wen Hou et al. 2016, RAA, 16, 138).

Hypervelocity stars

Hypervelocity stars have velocities that exceed the escape velocity of the Galaxy. They were first predicted by Hills (1988) as a consequence of the tidal disruption of tight binary stars by the central massive black hole of the Galaxy. The first hypervelocity star was discovered by Brown et al. (2005).

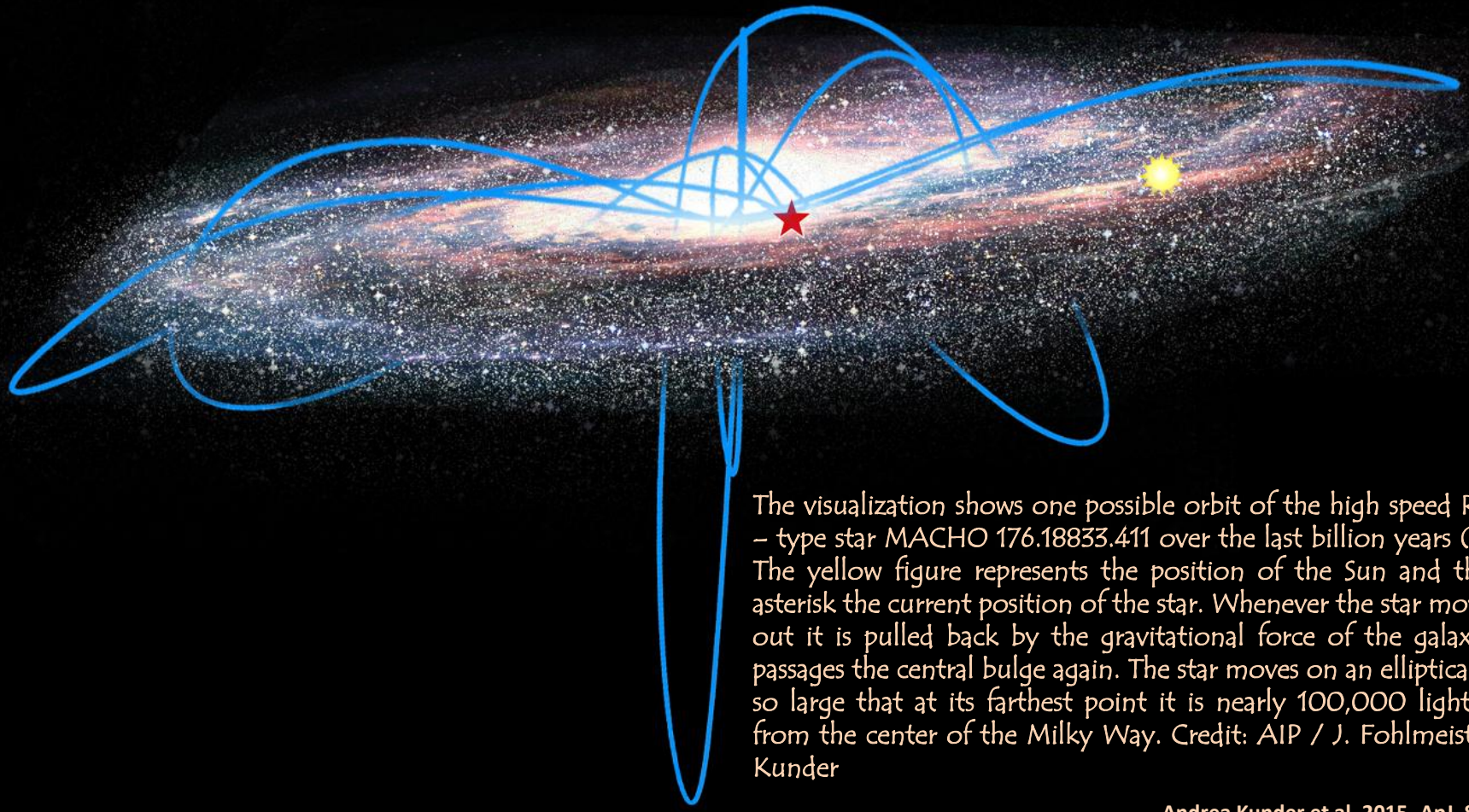

The visualization shows one possible orbit of the high speed RR Lyr – type star MACHO 176.18833.411 over the last billion years (blue). The yellow figure represents the position of the Sun and the red asterisk the current position of the star. Whenever the star moves far out it is pulled back by the gravitational force of the galaxy and passages the central bulge again. The star moves on an elliptical orbit so large that at its farthest point it is nearly 100,000 light years from the center of the Milky Way. Credit: AIP / J. Fohlmeister, A. Kunder

Andrea Kunder et al. 2015, ApJ, 808, L12.

Hypervelocity stars

J091206.52+091621.8 (LAMOST-HVS1) is the first hypervelocity star discovered in the LAMOST spectroscopic survey (Zheng Zheng et al. 2014)

LAMOST-HVS1 is a bright (~13 mag) and close (heliocentric distance of ~13 kpc) HVS with the heliocentric radial velocity of about 620 km s^{-1} and the Galactocentric radial velocity component of ~477 km s^{-1}.

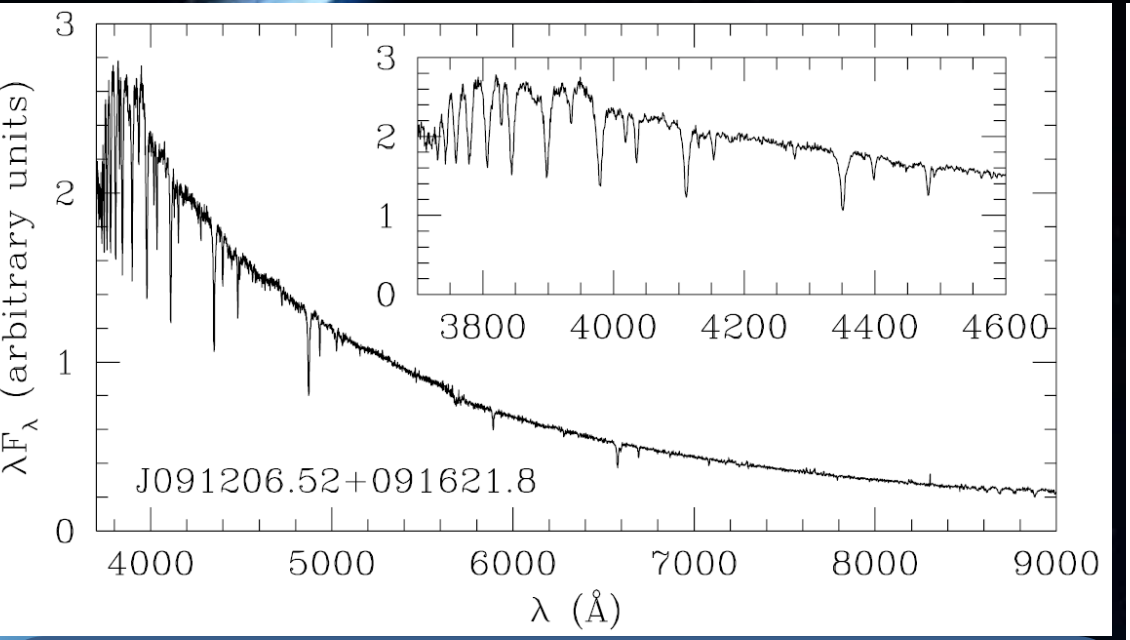

Spectrum of LAMOST-HVS1 taken with the Guo Shoujing Telescope. The inset shows a close-up view of the blue end of the spectrum (Zheng Zheng et al. 2014).

Jing Zhong et al. (2014): a catalog of 28 high velocity star candidates from the LAMOST DR1.
Yin-bi Li et al. (2015) : a catalog of 19 high velocity star candidates of spectral type F, G, or K from the LAMOST DR1.

Table 1
Properties of LAMOST-HVS1

	J091206.52+091621.8
Position (J2000)	$(\alpha,\ \delta) = (138.^{\circ}027199,\ 9.^{\circ}272725)$
	$(l,\ b) = (221.^{\circ}099564,\ 35.^{\circ}407261)$
Magnitudes	$g = 12.91$ $r = 13.22$ $i = 13.50$
	$B = 12.96$ $V = 13.06$ $J = 13.36$
	$H = 13.43$ $K = 13.53$
Distance	13.4 ± 2.2 kpc (Heliocentric)
	19.4 ± 2.1 kpc (Galactocentric)
Radial velocity	$v_{r\odot} = 620 \pm 10\,\mathrm{km\,s^{-1}}$
	$v_{\mathrm{rf}} = 477 \pm 10\,\mathrm{km\,s^{-1}}$
Proper motion (mas yr^{-1})	$(\mu_\alpha \cos\delta,\ \mu_\delta)$
	$(-4.0 \pm 0.7,\ -4.9 \pm 1.2)$ [UCAC4]
	$(-2.5 \pm 1.9,\ -1.2 \pm 1.9)$ [PPMXL]
	$(0.9 \pm 1.9,\ \ 0.9 \pm 1.9)$ [cPPMXL]
Spectral type	B
T_{eff}	$(2.07 \pm 0.12) \times 10^4$ K
$\log[g/(\mathrm{cm\,s^{-2}})]$	3.67 ± 0.19
[Fe/H]	-0.13 ± 0.07
Mass	$9.1 \pm 0.7\,M_\odot$


Thank you for attention!
Credit: Chinese Academy of Sciences